ALEPH-TPC NOTE # 86-01
7 January, 1986

R.C. Jared, U. of Wisc.

G. Sinnis, U. of Wisc.

M. Takashima, U. of Wisc.

A SIMULATION STUDY OF TPC PULSES

A detailed simulation study of pulses that originate from the TPC will be described. The effects that introduce error in coordinate finding and its implications on the TPC calibration system will be evaluated.

1.0 Introduction

A simulation study was performed to determine if the calibration system is adequate to calibrate the various types of pulses originating from the TPC. Parameters such as Landau fluctuations, diffusion, noise, phase and track angles were varied to see how they affect the chamber pulse shape and ultimately the position resolution. The present calibration system was constructed to pulse the pre-amplifiers with a pulse modeled from a $\Theta = 90^{\circ}$ straight track. This calibration pulse was

applied to the simulated TPC chamber pulses to determine if good position resolution could be maintained.

2.0 The TPC simulation program

A program has been developed to provide a detailed simulation of the response of the ALEPH TPC [1]. This section describes the underlying physics processes which have been considered, from the production of ionization along a path of a track to the recording of the digitized signal. The physical processes considered are :

1) The simulation of energy loss in the detector and the formation of clusters of electrons.

2) The transport of the clusters through the fields to the sense wires on the endplates.

3) The formation of avalanches at the sense wires.

4) The coupling of the avalanches to the pads.

5) The electronics shaping and amplification of the charge deposited on the wires and pads.

6) The addition of electronic noise to the signals.

7) The digitization.

The program takes as input track elements which consist of a starting location, direction cosines, a path length, a time of flight, a charge, a mass and an absolute momentum along with the track number. This allows the input of full events in the TPC from programs such as GEANT3 or to input one or several track elements defined by the user.

2.1 dE/dx Simulation

The aim is to generate realistically the clusters of electrons formed by the passage of a charged track through the TPC gas composed of 90% argon and 10% methane. A charged particle will lose energy through excitation and ionization as it traverses the gas. If an ionized electron has enough kinetic energy, it can produce secondary ionization. The result is clusters of electrons formed along the path of the original charged particle. If a primary electron is above a certain energy, it is called a delta ray. Delta rays can have sizeable path lengths in the TPC gas and are therefore treated in a special way.

The dE/dx observed varies in two ways with the gamma of the ionizing track. The number of ionizations per unit length and the distribution of energy transferred per ionizing collision changes. The

net effect is that both the number of clusters formed per unit length and the distribution in sizes of the clusters vary. In this simulation, only the number of clusters formed is varied. This is a good approximation up to a gamma of about 100 [2]. For gamma values larger than this, the number of collisions per unit length is scaled from its true value to account for the changing cluster size distribution.

To simulate the dE/dx of a charged particle passing through the gas, a primary electron is generated at intervals given by a Poisson distribution

$$P_N(k) = N^k \cdot e^{-N} / k!$$

where $P_N(k)$ is the probability of having k interactions per unit length given a mean of N.

If the primary electron has energy less than the cutoff set for delta rays, then all secondary electrons are positioned at the point of the primaries. The cutoff is chosen in such a way that for non-deltas, the smearing of the cluster due to diffusion dominates the smearing from the flight path of the primary electrons. The number of secondaries is generated so as to agree with Table 1 (from Ref. 2).

If the primary electron has an energy larger than the cutoff set for delta rays, the energy distribution of the primaries is assumed to follow a Rutherford distribution

$$dN/[dxdE] = [(z/A)\cdot k\rho] / \beta^2 E^2 \ MeV^{-1} cm^{-1}$$

$$k = .154 \ MeV/g\text{-}cm^{-2}$$

$$\rho = .00178 \ g/cm^{-3}$$

where z,A are the average charge and atomic number of the argon-methane mixture.

This is a good approximation if the minimum energy cutoff for the delta ray is high enough (See Ref. 2). If the delta ray has an energy above 1 MeV, it is treated as a track by the main tracking program.

The flight path of the primary electron from a delta ray is parameterized such that the path length follows the following formula :

$$L(cm) = 100 \times P^3 \text{ where P is in MeV.}$$

This parameterization was arrived at by determining how much path length is would take for an electron to "thermalize" or to fall below the delta ray cutoff. Electrons of different momenta were passed through the dE/dx simulation and their path length was measured as the sum of the distances between ionizing interactions until they fell below the minimum energy. Note that this is the total path length of the primary. Since the electron will undergo multiple scattering, the total length is reduced by a scaling factor. This simulation appears to be

valid in the range 2.5 KeV - 1 MeV. See Table 2 for the simulation results.

The angle (α) at which a delta ray is generated from the ionizing track is determined from momentum conservation. The angle about the track direction (β) is generated randomly. See Figure 1 for a definition of the angles.

The clusters resulting from the delta ray are deposited along a cylinder of radius depending on the component of the delta ray momentum perpendicular to the magnetic field. This radius is scaled up slightly to account for multiple scattering. Clusters are deposited in z steps along the cylinder with cluster sizes depending on the amount of energy lost between steps by the delta ray. The r-ϕ position of the cluster along the cylinder is determined randomly. For a given energy loss per unit length, the amount of energy deposited between steps is easily calculated. The cluster size is determined from the work function :

$$N(K) = K/W(K) \simeq (K - K_0) / W_0,$$

where N is the cluster size,

K is the kinetic energy transferred,

w is the work function.

The values for K_0 and W_0 are 15.8 eV and 26.4 eV respectively. The size of the cluster is smeared using the Fano factor to determine the width in cluster size :

$$(dN)^2 = F \cdot N$$

where F ranges from .18 to .19.

Figure 2 shows how a delta ray can affect a wire. A hundred events generated using the LUND generator and tracked by GEANT3 have been processed by the simulation described above (with the delta ray simulation off). In Figure 3, the number of clusters formed formed per centimeter of track length as a function of the track momentum was plotted. The bands from electrons, pions, kaons and protons are clearly visible.

2.2 Transport

The clusters that are created in the dE/dx process are then transported to the endplate. The electrons are transported one at a time (up to a maximum number of electrons per cluster). The electrons

are first transported to the gating grid taking into account diffusion according to the following formulas :

$$\Delta t = \sigma_l \cdot \sqrt{d} \cdot \xi \; / \; v_d$$

$$\Delta s = \sigma_t \cdot \sqrt{d} \cdot \xi$$

where Δt is the shift in the drift time,

Δs is the transverse shift along x or y,

d is the drift distance,

v_d is the drift velocity,

σ_l is the sigma for longitudinal diffusion,

σ_t is the sigma for transverse diffusion,

ξ is a normally distributed random number.

Beyond the gating grid, a parameterization depending on the voltage configuration is used to determine where the electrons will hit the sense wires. The electrons are also shifted due to the E x B effect. This shift has been parameterized for different voltage configurations and with the magnetic field on and off. The simulated E x B shift can be seen for a particular configuration in Figure 4.

2.3 Avalanche

Each electron arriving at the sense wire generates an avalanche which is on the order of $\sim 10^{-4}$ electrons for the forseen operating voltages. The size of the avalanche is generated using a Polya distribution :

$$f(z) = [z^{\Theta} \cdot e^{-(\Theta+1)z} \cdot (\Theta+1)^{(\Theta+1)}] \; / \; [\Gamma \cdot (\Theta+1)]$$

where z is the ratio of the charge in the avalanche to the mean charge per avalanche. Θ is about .5 (See Ref. 2).

2.4 Coupling to Pads

An expression that represents the charge induced on a pad is given by the Gaussian shaped "pad response function" [3]. This function is expressed as

$$P = A \cdot \exp(-w^2 \; / \; 2\sigma_w^{\,2})$$

where A is the amplitude, w is the distance along the pad width to the pad center, and σ_w is dependent upon geometrical factors such as pad

size, pitch and wire spacing. By laser measurements and also by Monte Carlo studies, σ_w has been found to be ~.32 mm (See Ref. 3).

Ratios of the pad response functions from several pads lead to algorithms that find the r-ϕ coordinate. The "three pad algorithm" [4] uses the pulse heights from three contiguous pads in a local maximum on a pad row. The pad with the largest amplitude and its 2 adjacent neighbors are used. This algorithm is given by

$$\phi = \phi_1 + [\sigma^2 \cdot \ln(P_1/P_2) - .5 \cdot \Delta^2] / R \cdot \Delta$$

where

$$\Delta = R \cdot (\phi_1 - \phi_2)$$

$$\sigma^2 = \Delta^2 / [2 \cdot \ln(P_1/P_2) + \ln(P_2/P_3)]$$

P_1,P_2 and P_3 are the signals from the three pads, R is the radius of the pad row and ϕ_1 and ϕ_2 are the phi positions of the pads with signals P_1 and P_2. This algorithm works best if the center of the avalanche lies near the center of a pad. If the avalanche is positioned in or near a gap between pads, the induced charge is shared mainly by just two pads and the three pad algorithm breaks down. In this case, only the pads with the 2 largest amplitudes will be used. This is called the "two pad algorithm." The algorithm can be expressed by

$$\phi = (\phi_1 + \phi_2)/2 + \sigma^2 \cdot \ln(P_1/P_2)/[R \cdot (\phi_1 - \phi_2)]$$

where $$\sigma = \sigma_w + P_r \ ,$$

$$P_r = (P_2/P_1) \times (P_3/P_1) \ .$$

2.5 Electronic Shaping and Amplification

The charge generated on the wires and pads from the avalanche process is passed through a simulation of the amplification and shaping that occurs in the TPC electronics. A functional representation of the response of the electronics to an input of electrons is calculated using Laplace transforms [5]. The convolution integral of input electrons with this function called the "input response function" provides the simulated output from the electronics.

If a single electron is input into the electronics, the resultant output pulse is in the semi-Gaussian shape of the input response function. The output pulse from the electronics of a chamber pulse is given by

$$S_0(T_m) = \int_{-\infty}^{T_m} S_i \cdot W(t)\, dt$$

where $S_0(T_m)$ is the output signal at time T_m ,

S_i is the input signal at a time $t \leq T_m$,

$W(t)$ is called the weighting function.

The weighting function W(t) is related to the input response function h(t) by $W(t) = h(T_m - t)$. The above formula expresses that any signal measured at some specific time T_m is formed from the superpositions of the responses of all electrons arriving in the electronics before the time T_m. Each electron is weighted according to the time of arrival of the electron before the time T_m.

2.6 Electronic Noise [6]

The two predominant sources of noise in the TPC electronics originate in the pre-amplifiers for the cathode pads and sense wires. See Figure 5 for an equivalent schematic of the pre-amplifier.

The first source is called "Johnson noise" or noise that is produced by the thermal motion of electrons in the resistors that are in parallel with the input. This type of noise also referred to as "parallel noise" originates primarily in the feedback resistor R_f for the TPC pre-amplifier. The second noise source resides within the FET of the operational amplifier. The fluctuations of the electrons flowing in the conducting channel of the FET causes a considerable contribution to the total noise at the output of the electronics. This type of noise is dependent on the resistance of the conducting channel which is given by $R_s = 1/g_m$, where g_m is the transconductance of the FET. This FET noise can be modeled by replacing the true "noisy" FET with a series

combination of a perfect, noiseless FET and a resistor of value R_s. This noise is then often referred to as "series noise."

The thermal noise produced in resistors can be represented by either a current source of noise electrons in parallel with a noiseless resistor or by a voltage source of noise in series with the noiseless resistor [7]. The mean squared noise voltage and current are given as

$$\overline{e_n^2} = 4KTR \quad \text{and} \quad \overline{I_n^2} = 4KT/R.$$

Traditionally, parallel noise is represented by a current source while series noise is usually depicted as a voltage source of noise. The schematic of the pre-amplifier can then be redrawn with a noiseless operational amplifier and a noiseless feedback resistor with a current noise source for parallel noise and a voltage noise source for series noise. See Figure 6.

The noise electrons produced by the current and voltage sources of noise are amplified and shaped separately from the signal electrons produced in the TPC. The noise spectrums from the two sources are added linearly to the chamber signal after the shaping stage.

The expressions given above for a current and voltage noise sources calculate only the mean squared noise current and voltage per Hz at the input to the electronics. An algorithm to produce a noise spectrum for the TPC electronics must still be formulated.

Since the pre-amplifier is a charge sensitive device, the noise input must be in the form of electrons. The current source depiction of noise will be the more convenient of the two types of representations. The series noise voltage source will then be transformed into a current source via a Thevenin equivalence. The general procedure that follows is to calculate the mean number of noise electrons per second for parallel and series noise and then distribute them randomly over a given time interval. The distributed electrons are then convoluted with the input response function.

The fluctuations in a current I can be modeled by a series of randomly distributed current impulses given by $\delta(t)q_0$ [8] (where $\delta(t)$ is the Dirac delta function and q_0 is the electron charge). The average rate of these impulses is given by $n(I) = I/q_0$. This train of delta pulses can be shown to be equivalent to white noise with a uniform spectral density of a mean squared value $2nq_0^2$ per Hz and a DC component of value nq_0 [9]. A noise current source can then be alternatively represented as a random sequence of delta pulses whose mean squared value is given by $\overline{I^2} = 2nq_0^2$. If this expression is equated to $\overline{I^2} = 4KTR$, the average rate of delta pulses n(I) can be determined. This rate will provide the average number of noise electrons input per second into the electronics.

The Parallel noise coming from the feedback resistor is easily depicted as a current generator of noise in parallel with a noiseless feedback resistor. The mean squared number of noise electrons of this type is calculated with the procedure outlined above. For convenience,

a time period of one second is divided into 10 ns bins. The average number of noise electrons per second is first distributed evenly into these 10 ns bins. This flat, even distribution, in fact, constitutes the DC level of the eventual fluctuating noise spectrum. A random noise distribution is obtained by varying the number of electrons per bin by a normally distributed random number. The peak of the normal distribution lies at the value of the DC level and the sigma is the square root of the value of the DC level. This array of input parallel noise can then be convoluted with the input response function to produce a noise spectrum at the output of the electronics.

Series noise has traditionally been represented as a voltage source of noise. Recall that the pre-amplifier requires electrons, so a Thevenin equivalence to transform this source into a current source must be performed. The resulting mean squared current for series noise will then be

$$\overline{I_n^2} = \overline{e_n^2}/Z = 4KTR_S \; / \; [R_f/(R_f C_t S + 1)]^2$$

where C_t is the total input capacitance,

S is a differential operator.

By some algebraic manipulation, this equation becomes :

$$\overline{I_n^2} = 4KTR_sC_t^2 \cdot [S^2 + 1/(R_fC_t)^2 + ...]$$

The second term in the parentheses is effectively zero and can be ignored.

The process of finding the average number of electrons per second is more complicated for the series noise case. During the Thevenin equivalence transformation, the number of input electrons for series noise was artificially altered to compensate for the transformation. The formalism of the Thevenin equivalence provides mathematically correct results for mean squared calculations. However, the crucial aspect of this time domain algorithm for noise is that the number of electrons be preserved. The expression for mean squared current for series noise is then rewritten as

$$\overline{I_n^2} = 4KT/R_s \cdot (R_sC_t)^2 \cdot (S^2 + ...)$$

The term $4KT/R_s$ is used to calculate the average number of series noise electrons per second. After these electrons are randomly distributed in their respective 10 ns time intervals, the number of electrons in each bin is weighted by the factor R_sC_t. Instead of altering the number of electrons, the amount of electrons is conserved and the weight of each electron is changed. In the delta impulse model of noise, this

corresponds to keeping the rate n(I) constant and changing the value of the weight q_0.

The differential operator S in the expression for mean squared current arises from the input capacitors in the pre-amplifiers. The operator imposes the requirement that the input series noise electrons be convoluted, not with the input response function, but with the derivative of the input response function.

The number of mean squared parallel and series noise electrons at the output of the TPC electronics can be calculated analytically by the respective expressions :

$$\overline{N_p^2} = [2KT/R_p q_0^2] \cdot \int_{-\infty}^{\infty} W(t)^2 dt$$

and

$$\overline{N_S^2} = [2KTR_S C_t^2/q_0^2] \cdot \int_{-\infty}^{\infty} W'(t)^2 dt$$

where q_0 is the electron charge,

R_S is the equivalent series resistance,

R_p is the equivalent parallel resistance,

C_t is the total input capacitance,

W(t) is the weighting function,

K is Boltzmann's constant

T is the temperature.

Calculations using the formulas above produce 175 mean squared electrons for parallel noise and 272 mean squared electrons for series noise.

Simulated noise spectrums were created for parallel and series noise using the time domain algorithms. The spectrums were sampled every .5 μs to determine the mean squared number of electrons. The number of noise electrons from the parallel noise spectrum was found to be 176, while the number from the series noise spectrum was 277. The amount of correlation in the noise samples was also calculated. The correlation length for parallel noise was on average 470 ns or about a shaping time of the shaping network. The length for series noise was about half a shaping time. These correlation times will be seen to have a significant effect on the behavior of the signal to noise ratio.

Long arrays (.01 secs) consisting of 10 ns bins were created for both parallel and series noise. The noise was added linearly to the chamber signal in the simulation after the shaping stage of the electronics chain. The sections of the noise arrays to be added to a given chamber signal were selected at random by a random number generator.

2.7 Digitization

In the digitization phase, the effects of differential non-linearity, gain variation, pedestals, and pedestal variation are taken into account. The digitization can be performed with either an 8 or 9 bit linear FADC or a combination of two 7-bit FADC's in parallel.

Figure 7 shows the pads hit from a typical 90 GeV event in the TPC. Figures 8 a and b show pulses form the simulation in two typical cases.

3.0 Results of the Pulse Simulation Study

A group of data sets consisting of digitized pulse shapes was created using the TPC simulation program. Each data set focused on chosen parameters such as diffusion, Landau fluctuations or noise in an attempt to understand the effects of these parameters on the position resolution. A convenient feature of the simulation program was the ability to selectively turn "on" or "off" these parameters. The simulated pulses were affected only by the parameters requested. All simulated TPC pulse were normalized to a calibration pulse from a 90^{0} straight track.

In parallel, a study of different algorithms that sample the digitized pulses was conducted. The influence of the sampling algorithms on the resolution with respect to the chosen parameters was measured.

The digitized pulses are the result of track elements produced by a 5 GeV pion. The track elements are centered in r-ϕ in all cases directly over the center of a pad. The pad utilized for these simulation tests lies in the center of the middle pad row in one of the six inner sectors. This pad then has the sense wires strung perpendicular to the length axis of the pad and is also immune to any edge effects which may occur close to a sector wall. The track elements are drifted from the center of the TPC where the drift distance is 100 cm. The range of polar angles studied is 0^{0}-50^{0} while the range studied in

azimuth is 0^0-30^0. The pulses are also studied at four phase orientations with respect to the digitizer clocks.

Separate data sets were created for noise, diffusion and Landau fluctuations. Six polar angles at $\phi = 0^0$ were examined for each case. A total of 200 pulses was created for each polar angle. A data set of the combined effects of all the parameters was also made. This set was produced with 800 pulses for each of the six polar angles. In addition, a study of ϕ angles at $\Theta = 0^0$, 30^0 and 50^0 was conducted. A total of 800 pulses were created for each of the ϕ orientations.

The resolution was calculated from the simulation data by comparing the coordinate constructed by the coordinate finding algorithm to the exact coordinate. The exact coordinate was calculated simply from the position of the center of the pad over which the track element was formed. The coordinate finding algorithm utilized the two or three pad algorithm depending on the application. If four pads in a pad row were above threshold, the three adjacent pads with the highest weight were used to construct the coordinate. If five or more pads were above threshold, then a simple geometrical center of the pads fired was used to calculate the r-ϕ position.

3.1 The Perfect Case

A data set consisting of pulses from the TPC with all effects "turned off" was first considered. Figures 9 a, b and c show the peak

amplitude of the pulse heights as a function of polar angle. The algorithm used for Figure 9a was simply the maximum ADC count in the pulse height. Figure 9b utilized the fitted parabola algorithm while Figure 9c was made from an interpolated parabola which fitted five points. It can be seen that the peak of the pulse height decreases as the polar angle is increased from the normal to the beam axis. This can be easily understood by the fact that as a track becomes more inclined, the time distribution for charge becomes wider. Less charge will be accumulated by a given digitizer bucket. For example, for this "perfect" case, all charge created from a track perpendicular to the beam axis arrives at the endplate simultaneously while charge from inclined tracks arrive with some Δt between consecutive ionization electrons. This time interval Δt obviously increases as the polar angle is increased. The general trend is for the pulse amplitude to decrease with increasing angle and also for the pulse to widen in time.

Figure 9d shows the variation of the sum of ADC counts in a pulse height with respect to polar angle. This method is referred to as the "area algorithm." The total number of ADC counts or the area under the pulse height can be seen to rise with increasing polar angle. In these perfect pulses, the interval between ionizations and the number of electrons per ionization are held constant. The charge can then be expected to rise as

$$Q \propto D / \cos\Theta$$

where Q is the charge produced

D is the pad length

Θ is the polar angle

Figure 9d can be seen to exhibit this $1/\cos\Theta$ behavior.

The error bars in the four figures represent the phase errors from the four phase orientations. The phase variations decrease for the peak finding methods with increasing polar angle. The pulse widens with polar angle and in fact creates a "plateau" for these perfect pulses. See Figures 10 a and b for a comparison of a pulse from $\Theta = 0^\circ$ and one from $\Theta = 50^\circ$. The width for a pulse at $\Theta = 50^\circ$ is on the order of 12-14 digitizer bins or about two shaping times. Pulses of this length will no longer exhibit a semi-Gaussian shape and will be flattened near the peak region. The phase variations are then smaller for increasing polar angle because of the creation of this plateau region. In any case however, the maximum variation introduced for all angles is only ~.3%. Table 3 shows numerically the variations of the four algorithms with polar angle with their respective phase errors.

3.2 Pulses with the addition of Noise

The noise spectrums from parallel and series noise were added to the "perfect case" pulses to determine their effects on the position

resolution. The digitized pulses were once again sampled using the four algorithms mentioned in the last section. Table 4 shows the resolutions obtained with the noise contributions. The sigmas of the resolutions are given with the statistical and phase errors included.

The peak finding algorithms worsen with increasing polar angle while the area algorithm shows the opposite trend. The factor which determines the resolution in all cases is the signal to noise ratio. This quantity can be found to be intimately associated with the correlation lengths of the noise spectrums. Recall that the parallel noise correlation length extends to about a shaping time or ~500 ns while the series noise correlation length lasts for approximately half a shaping time.

The top ADC count algorithm uses only one 80 ns digitizer bin while the parabola and the five point interpolated parabola use three and five bins respectively. The effect of noise on the resolution is directly associated with the level of correlation of the noise spectrums in the bins used to sample a pulse. Since this number of bins stays uniform for the peak finding algorithms regardless of the shape and length of the pulse, the total amount of noise which affects the resolution when measuring these pulses should remain constant over a sweep in polar angle. However, the amplitude of the pulse heights decreases with increasing polar angle because of the geometrical arguments outlined in the last section. The signal to noise ratio should then decrease and consequently the position resolution should worsen with increasing polar angle. This in fact corresponds to the results.

A comparison of the peak finding algorithms shows that the top adc count method exhibits the poorest resolution. This is because this algorithm possesses 100% correlation in both parallel and series noise. The parabola method which uses three digitizer bins is shown to be worse than the five point interpolated parabola. At three bins, which corresponds to 240 ns, all bins will be correlated in both parallel and series noise. The five point method also has all bins correlated in parallel noise, but , at this point, most of the series noise is anti-correlated. Since series noise has a higher R.M.S. contribution than the parallel series, the increase in correlated parallel noise bins would be more than offset by the loss of correlated series noise. In fact, series noise has a 50% higher contribution, so it would be expected that the five point interpolated method exhibit an improved resolution over the "normal" three point method. These peak finding algorithms show that the effect of noise on the resolution depends not on the number of bins used, but the level of correlation of the noise in these bins.

The area algorithm can be seen to improve with increasing polar angle. For the sake of argument, if the noise is 100% correlated over the entire spans of the pulses, simple geometrical reasoning would indicate that the resolution should worsen with an increasing polar angle. The argument is that the charge accumulated on a pad increases $\propto 1/\cos\theta$ while the time for this accumulation and therefore the number of digitizer bins $\propto \tan\theta$. However, the measured resolution shows the opposite trend. The explanation of this result lies in that while the

the amount of charge grows with polar angle, the noise spectrums oscillate with cycle times depending on the correlation lengths.

The number of digitizer bins used by the area algorithm ranges from seven to twelve bins with increasing polar angle. At seven bins, with average correlation lengths of ~500 ns and ~250 ns for parallel and series noise, the parallel noise is on average past half a cycle and is starting to anti-correlate. The series noise is on average already 60 ns past a full cycle. After 10 digitizer bins, multiple cycles for both noise spectrums must be considered. So it can be seen that as the signal charge increases as $1/\cos\theta$, the noise spectrums oscillate and so their effects do not increase linearly with the number of digitizer bins. The signal to noise ratio is then dependent on the rising amount of charge and on the noise determined by the phases of the oscillating spectrums with respect to the number of digitizer bins used. The resolution improves for the area algorithm with polar angle because of the choice of the shaping time of the electronics. The shaping time is short enough such that the noise becomes cyclic over the number of digitizer bins used to sample the pulse.

3.3 Pulses with Diffusion

The effects of diffusion on the position resolution were next studied. In order to eliminate Landau fluctuations, the intervals between ionizations along a track and the number of electrons per

ionization were held fixed. The interval was set to the Poisson mean of .1 cm. The number of ionization electrons per ionization was given to be the average number of electrons per ionization in the TPC gas mixture or three electrons per ionization. The sigma for transverse diffusion was set at 58 μm per electron per square root cm of drift length. Table 5 gives the position resolutions obtained for pulses with only diffusion.

The results show that higher statistical significance has to be achieved before any concrete statements can be made. However, in general, the peak finding methods appear to produce worse resolution with increasing polar angle while the area algorithm seems to attain a better resolution with increasing angle.

A track which traverses the center of a pad lengthwise will induce pulses primarily on the central pad and its two adjacent neighbors. Naively, it would be expected that the pulse heights on the three pads would be of different amplitudes due to the different capacitive coupling, but have the same shape. In other words, they would be mirror images of each other, but with different peak heights. The degradation of the peak finding algorithms indicate that this is not the case. Various effects must be displacing the ionization charge in r-ϕ such that the resolution decreases for these algorithms. These effects must also be coupled somehow to the polar angle such that they become more prounouced with an increase in this angle.

Processes which could displace the ionization are the angular and E x B effects. The ionization charge will be shifted in a direction depending on their locations with respect to the wire positions. If the

local concentration of charge along a track is not homogeneous, the angular and E x B shifts would distribute the charge unevenly in a sense wire cell. The degradation of the resolution would result mainly from the shift in the ϕ direction. Transverse diffusion will cause a degree of randomness in the local concentrations of charge and should therefore affect the r-ϕ resolution as described above. The addition of Landau fluctuations will be shown to significantly affect the resolution because of this effect.

An increased number of electrons which are used to sample a pad pulse should result in a better statistical averaging of the r-ϕ shifts. For any track element in the TPC, approximately 30 ionization electrons are expected to be created per cm track length. If a track is perpendicular to the beam axis and centered on a 3 cm long pad, 90 electrons will drift to the endplate and affect this pad. The number of electrons which affect a pad will increase with $1/\cos\theta$. With more charge, an increased number of statistically independent contributions will be used to construct a pulse. If the drift length is held constant and if all the charge created is used to sample the pulse, the resolution should improve with increased polar angle. From naive geometrical arguments and a σ_t of 58 μm, the expected position resolution with only diffusion effects can be calculated. At 100 cm drift length and 90 ionization electrons, the resolution can be calculated to be ~60 μm for a $\theta = 0^0$ track. For $\theta = 50^0$, the number of electrons that affects a pad increases to 140 and the expected resolution would be ~50 μm. These naive calculations, although not complete, illustrate that the variation of resolution can be understood by the increasing amount of charge.

The simulation data shows that the area algorithm appears to express this trend of improving resolution with increasing polar angle. This method samples all the digitizer bins of a given pulse height and therfore will use all the information available in a signal. The area algorithm can then benefit from the increasing number of statistically independent contributions and should attain better resolution with increasing angle.

The peak finding algorithms appear to worsen with polar angle. The distinctive feature of these methods is that the number of digitizer bins used to sample the pulse always remains constant independently of the shape and length of the pulse. As the polar angle is increased, it has been seen that the signal amplitude decreases and therefore the number of electrons per bin also decreases. These methods then ,in fact, reduce the number of independent contributions used to sample a pulse as the polar angle is increased. They cannot benefit from the $1/\cos\Theta$ dependence which increases the amount of charge that affects a pad because the number of bins that are used to sample is held fixed. The peak finding algorithms will be much more susceptible to the local fluctuations of charge positions and should produce worse resolution with increasing polar angle.

3.4 Pulses with Landau Fluctuations

Landau fluctuations can be seen to drastically reduce the resolution compared to the effects of diffusion and noise. See Table 6.

The peak finding algorithms again deteriorate the resolution with increasing polar angle while the area algorithm significantly improves. For example, at a polar angle of 50°, the area algorithm has an 80 μm improvement over the best peak finding algorithm.

The arguments used to understand these effects are identical to the ones used for diffusion. However, the magnitudes of the effects are now considerably larger because the distributions of charge along a track are now significantly more inhomogeneous. With Landau fluctuations, the interval between ionizations along a track and the number of electrons per ionizations is varied. If a given track is significantly inclined in polar angle, the fluctuations in the intervals between ionizations can cause large variations in the concentrations of charge in time. This results in deviations from the intended semi-gaussian shape of the shaping network. Figure 11 shows a pulse shape from a $\theta = 50^{\circ}$ track with Landau fluctuations. Notice that the pulse now possesses some "structure" due to the Landau effects. This pulse shape illustrates the degree to which the Landau fluctuations can affect the charge distribution. This uneven distribution coupled with the angular and E x B effects will lead to large r-ϕ coordinate errors for the peak finding algorithms. It should also be noticed that any type of fitting program will produce large errors for the z-coordinate with these types of pulses. The z resolution will be investigated in a subsequent study.

The area algorithm is insensitive to any structure in the pulse height. It is only dependent upon the total amount of charge deposited.

With increasing polar angle, more charge and therefore more statistically independent contributions to the signal will be used by the area algorithm. Since the number of digitizer bins used by the peak finding methods is held fixed, these algorithms can only produce worse resolution with increasing angle. This is because the amount of charge per bin has been seen to decline.

Figure 12 a, b, c and d show the independent contributions of noise, diffusion and Landau fluctuations using the four algorithms described previously. In each case, the resolution is dominated by Landau effects. The effects of noise are generally around 15-20 μm and therefore quite small. Diffusion can be seen to contribute an error of 60-70 μm. With the exception of noise at low polar angles, the area algorithm uniformly produces equal or better resolution than the three peak finding methods.

3.5 Pulses with Noise, Diffusion and Landau Fluctuations

A data set was compiled which included the combined effects of noise, diffusion and Landau fluctuations. The pulse heights were analyzed using the four previous algorithms as well as area algorithms with percentage thresholds. The position resolutions are given in Table 7 and Figures 13 a and b.

As expected, the peak finding algorithms produce worse resolution with increasing polar angle while the area method once again shows an improvement. The thresholds for the area method can be seen to significantly affect the resolution. The area method with a 5% threshold shows a slight improvement over the 0% case. At this level, the threshold eliminates some of the fluctuating noise baseline. The loss of ionization electrons to sample the pulse is offset by the elimination of the fluctuating noise spectrum. Above 5%, the resolution degrades because after the threshold rises completely above the noise, the loss of charge can only worsen the coordinate finding.

If Tables 6 and 7 are compared, the resolution for the area algorithm actually seems to improve with the addition of diffusion to the signal. The differences for the peak methods are not statistically significant. The reasons for this improvement are at the moment not exactly understood. A possible explanation is that the diffusion smooths the dominant effects of the Landau fluctuations. The diffusion spreads the ionization electrons in time as well as in r-ϕ. The distribution of charge will then be more uniform. If the Landau effects are attenuated, the E x B and angular effects will be less pronounced and spread the charge more evenly in a sense wire cell. However, this is only a conjecture. Further experimental and simulation studies are presently being conducted to understand how diffusion is related to the resolution in the TPC.

A data set was formed to study the resolution as a function of ϕ angle. This study was conducted at $\Theta = 0^{0}$, 30^{0} and 50^{0}. The results are shown in Figures 14 a, b, c and d.

In all cases, the the resolution rapidly degrades with ϕ angle. For example, the sampling algorithms already lose ~100 μm at $\phi = 5^0$ compared to the data at $\phi = 0^0$. As the ϕ angle is increased from the length axis of the pad, the angle at which the track crosses the wires is decreased. With decreasing angle, the pad signal is much more susceptible to Landau fluctuations affecting a given wire. Figure 15 exhibits how a single wire can "shift" the r-ϕ position depending on the location of the fluctuation. Another reason for the reduced resolution is that as the ϕ angle is increased, more pads will induce signals that are above threshold. As more and more pads are affected, the coordinate finding routines become increasingly confused. After more than five pads are fired, the coordinate finding relies on the geometrical average of the positions of the pads that have fired. This clearly leads to large r-ϕ errors.

At the lower ϕ angles, the area method produces the best resolution of the algorithms because, once again, it utilizes all the information that is available from the pulses. For the higher ϕ angles, the resolutions are essentially equivalent for all methods. At these angles, the coordinate finding routines have broken down and the geometrical centroids of the pads must be used. A procedure that will properly handle these situations must clearly be formulated.

The phase errors introduced by asynchronous sampling have been found to be on the order of half a percent. A procedure to calibrate the phase response of the TPC electronics would be trivial with the available hardware. However, because of the presence of Landau fluctuations, the phase relationship of a chamber pulse with respect to

the digitizer clocks is not obvious. The process of normalizing the chamber pulses to a phase calibration pulse would be difficult. Since the phase errors are not significant, it is recommended that the idea of a phase calibration be abandoned.

3.6 Conclusions

A study of the various pulse shapes in the TPC has been conducted. All pulses were normalized to a simulated pulse from a $\Theta = 90^{0}$ straight track. With the area algorithm, the position resolutions attained for a sweep in polar angle was ~110-140 μm. The sweep in phi angle was seen to be dominated by Landau fluctuations. The resolutions attained are clearly acceptable for the operation of the TPC. If the area algorithm is used, only the $\Theta = 90^{0}$ calibration pulse is necessary. With this method, any inclined track can be pictured as a series of consecutive $\Theta = 90^{0}$ tracks. Only the total charge is relevant for the area algorithm. This study has concluded that the present TPC calibration system will be sufficient to calibrate the electronics channels for the ALEPH TPC.

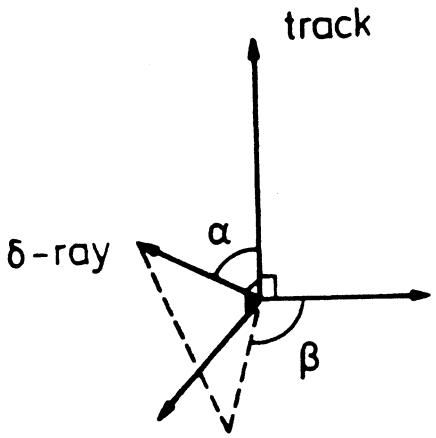

Figure 1

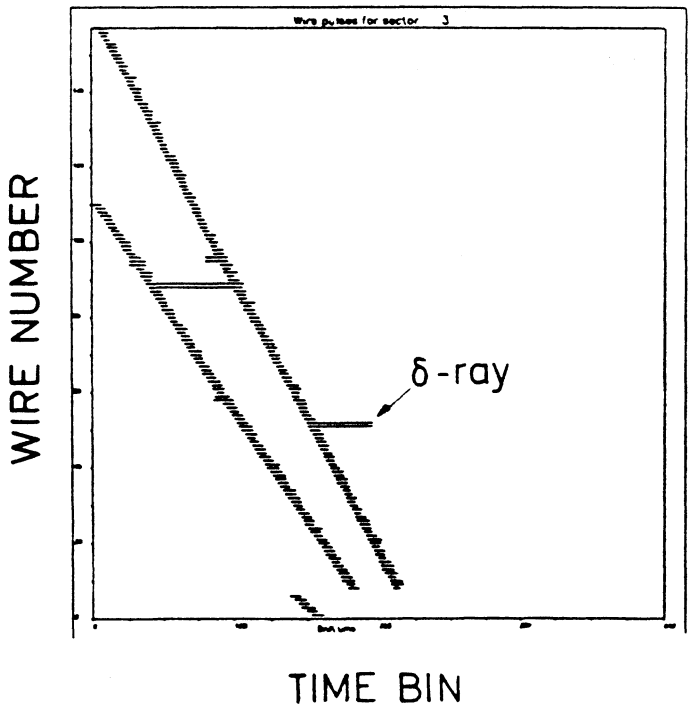

Figure 2

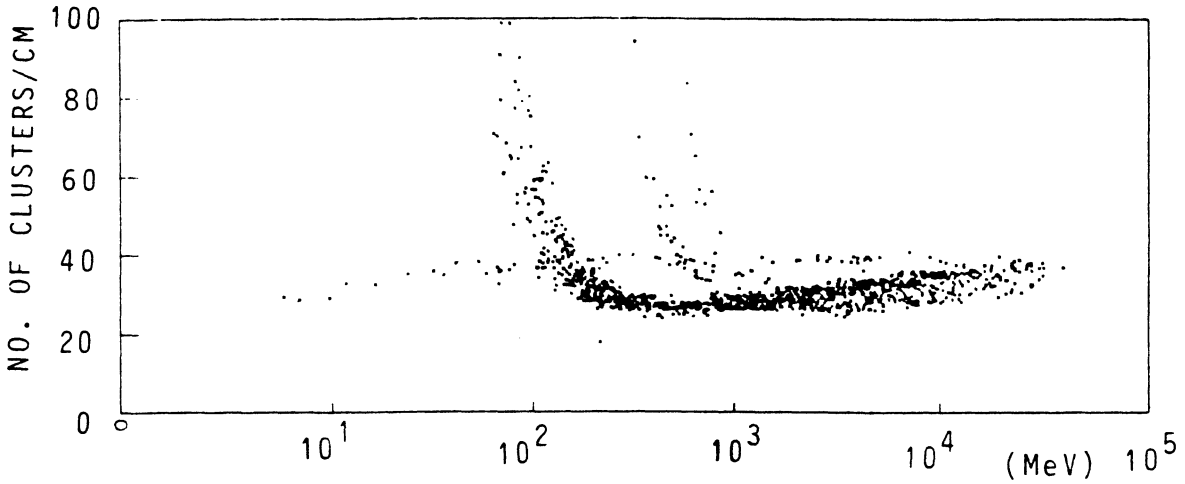

Figure 3

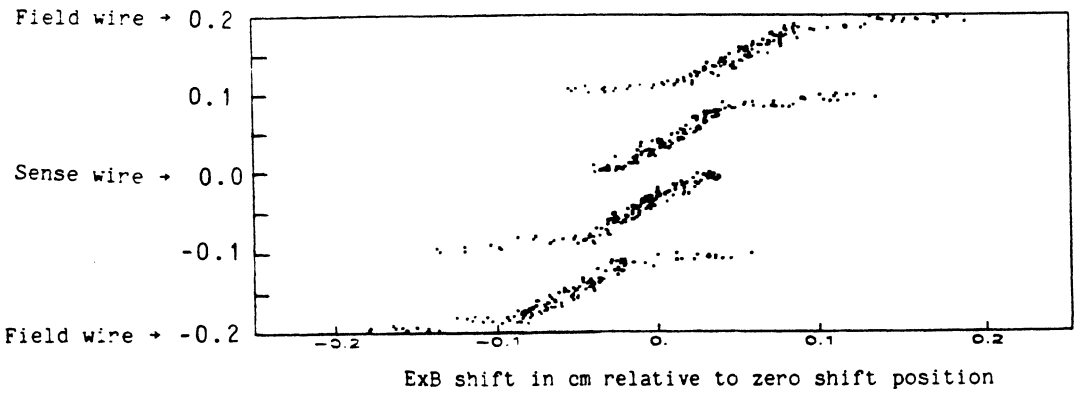

Figure 4

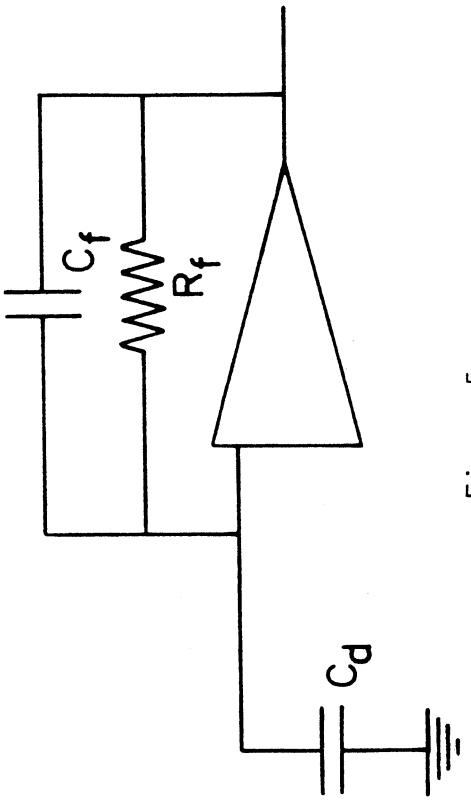

Figure 5

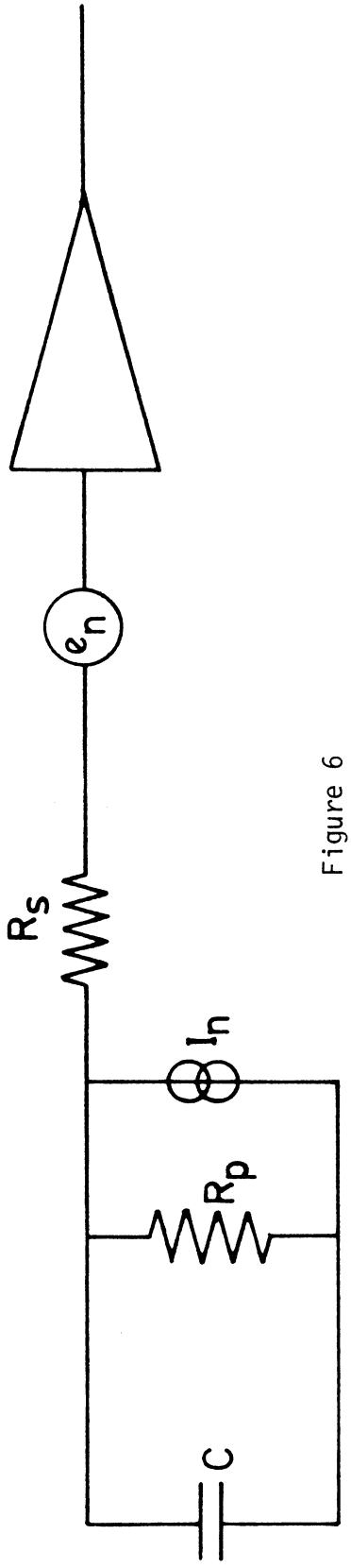

Figure 6

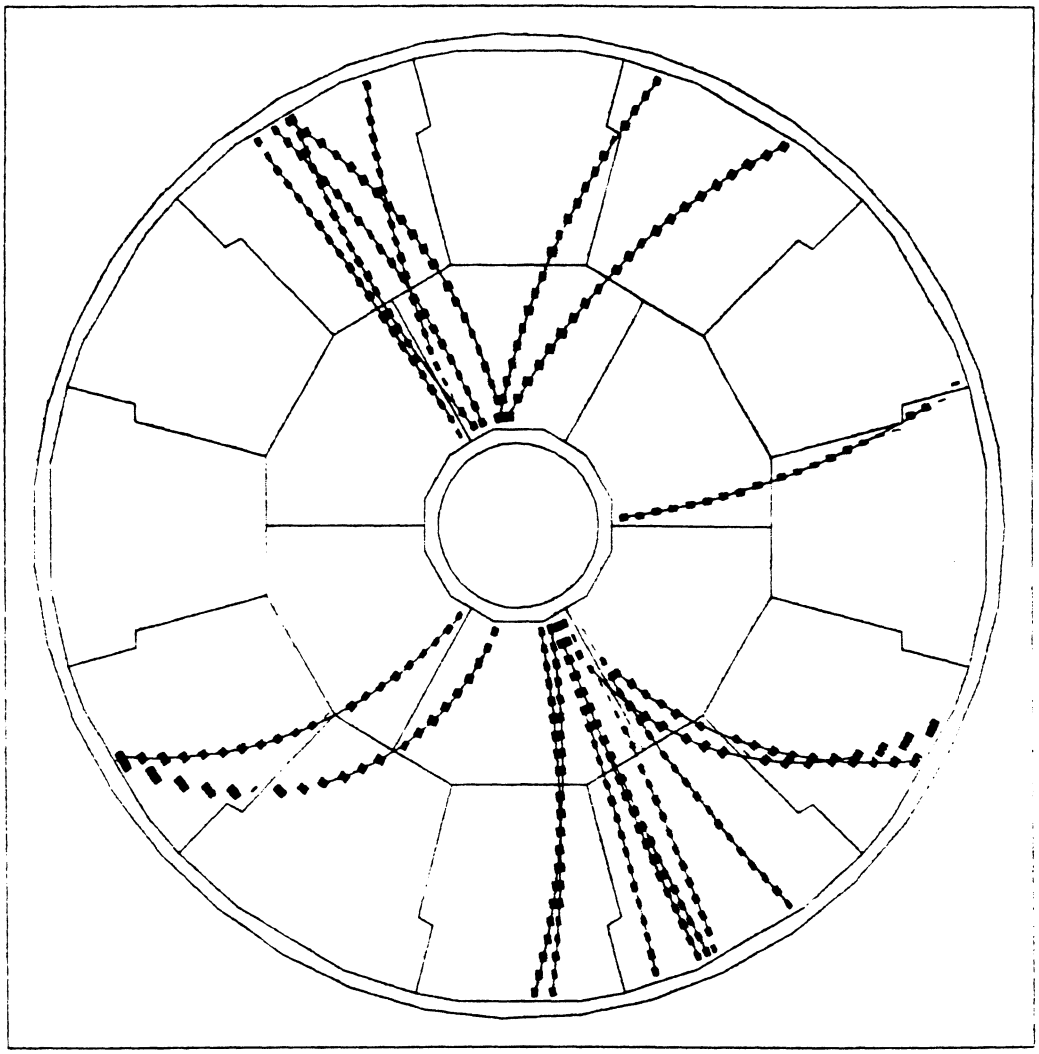

Figure 7

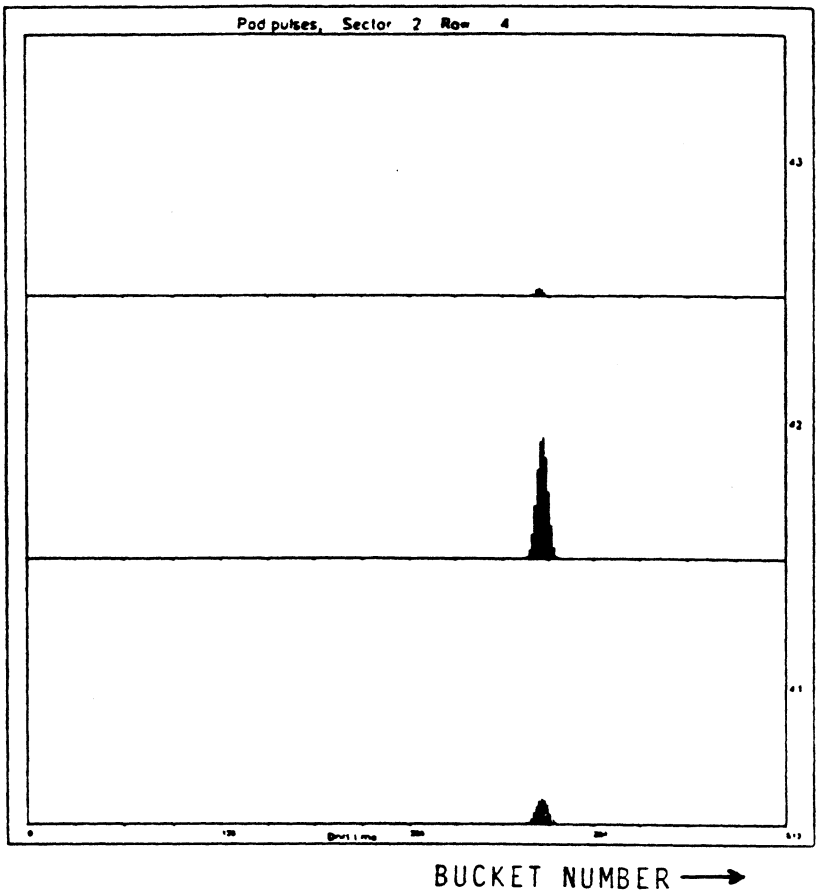

The signals on three adjacent pads resulting from a track passing over the center of a pad.

Figure 8a

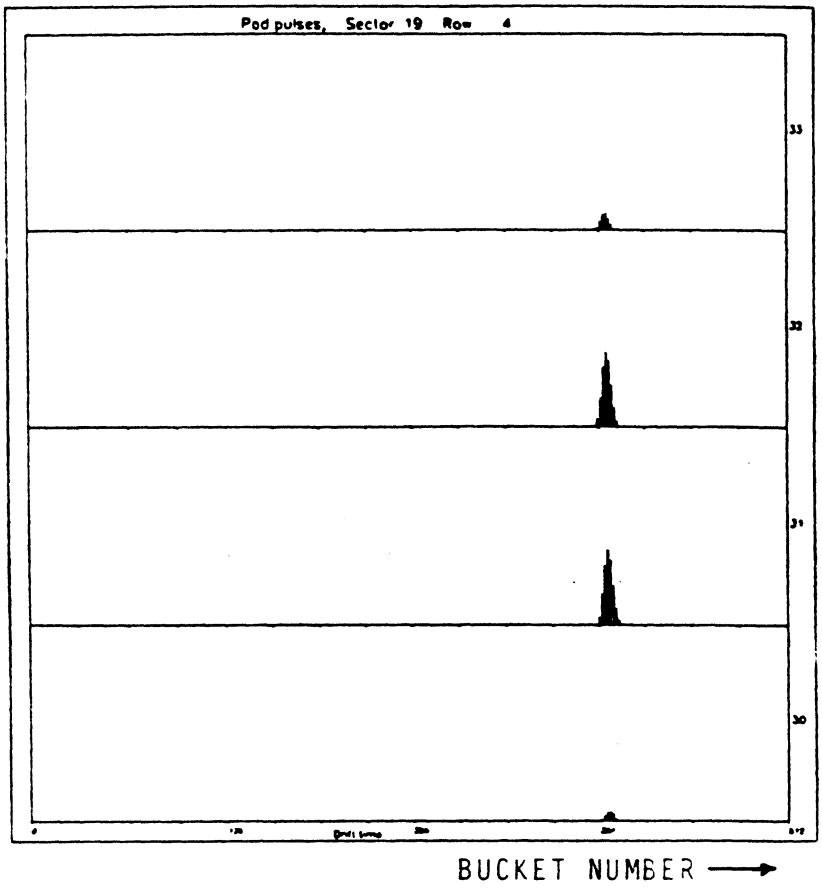

The signals on four adjacent pads resulting from a track passing between two pads.

Figure 8b

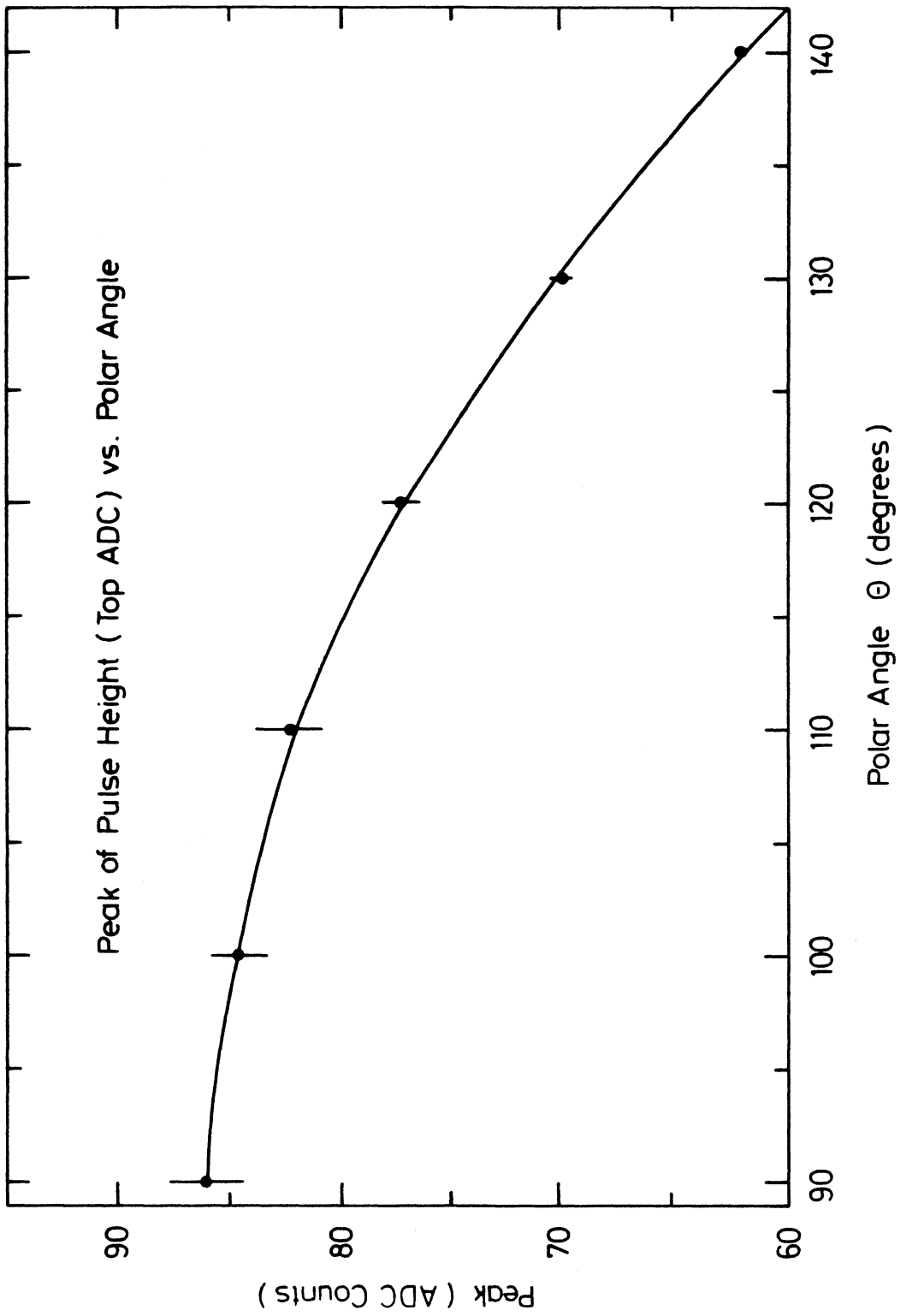
Peak of Pulse Height (Top ADC) vs. Polar Angle
Peak (ADC Counts)
Polar Angle Θ (degrees)
90
80
70
60
90
100
110
120
130
140

Figure 9a

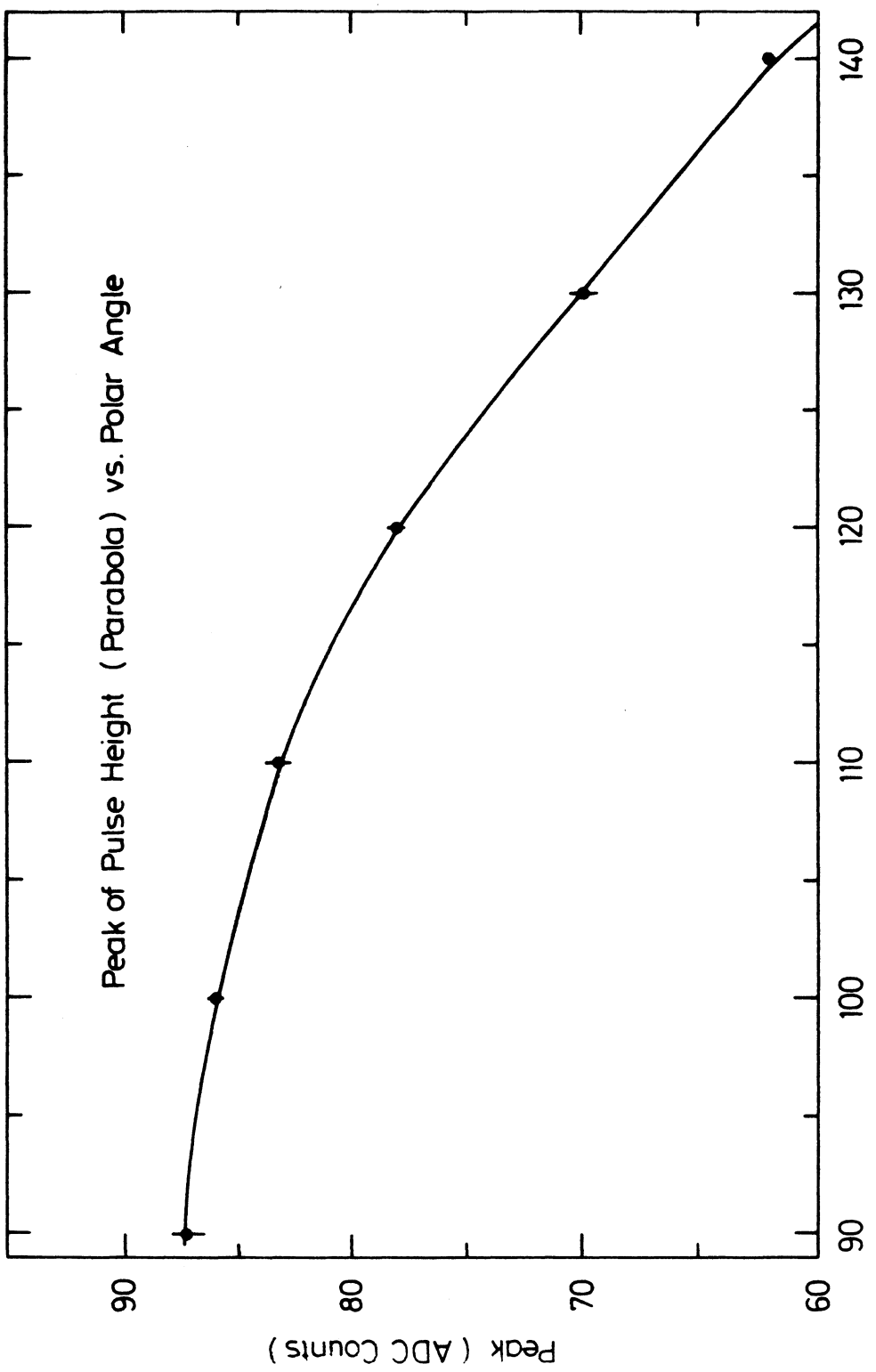
Peak of Pulse Height (Parabola) vs. Polar Angle
Peak (ADC Counts)
Polar Angle Θ (degrees)
60
70
80
90
90
100
110
120
130
140

Figure 9b

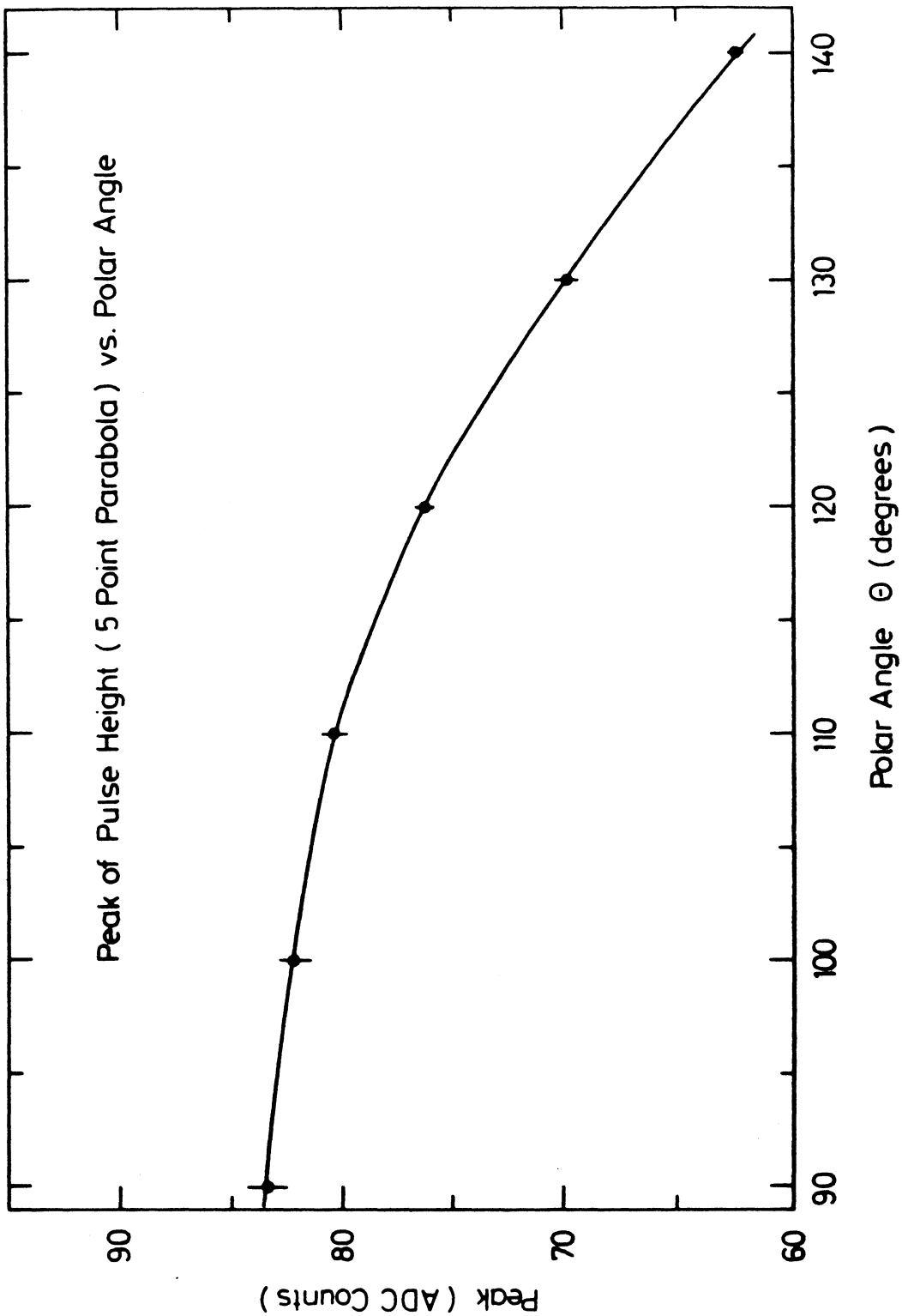
Peak of Pulse Height (5 Point Parabola) vs. Polar Angle
Peak (ADC Counts)
90
80
70
60
Polar Angle Θ (degrees)
90
100
110
120
130
140

Figure 9c

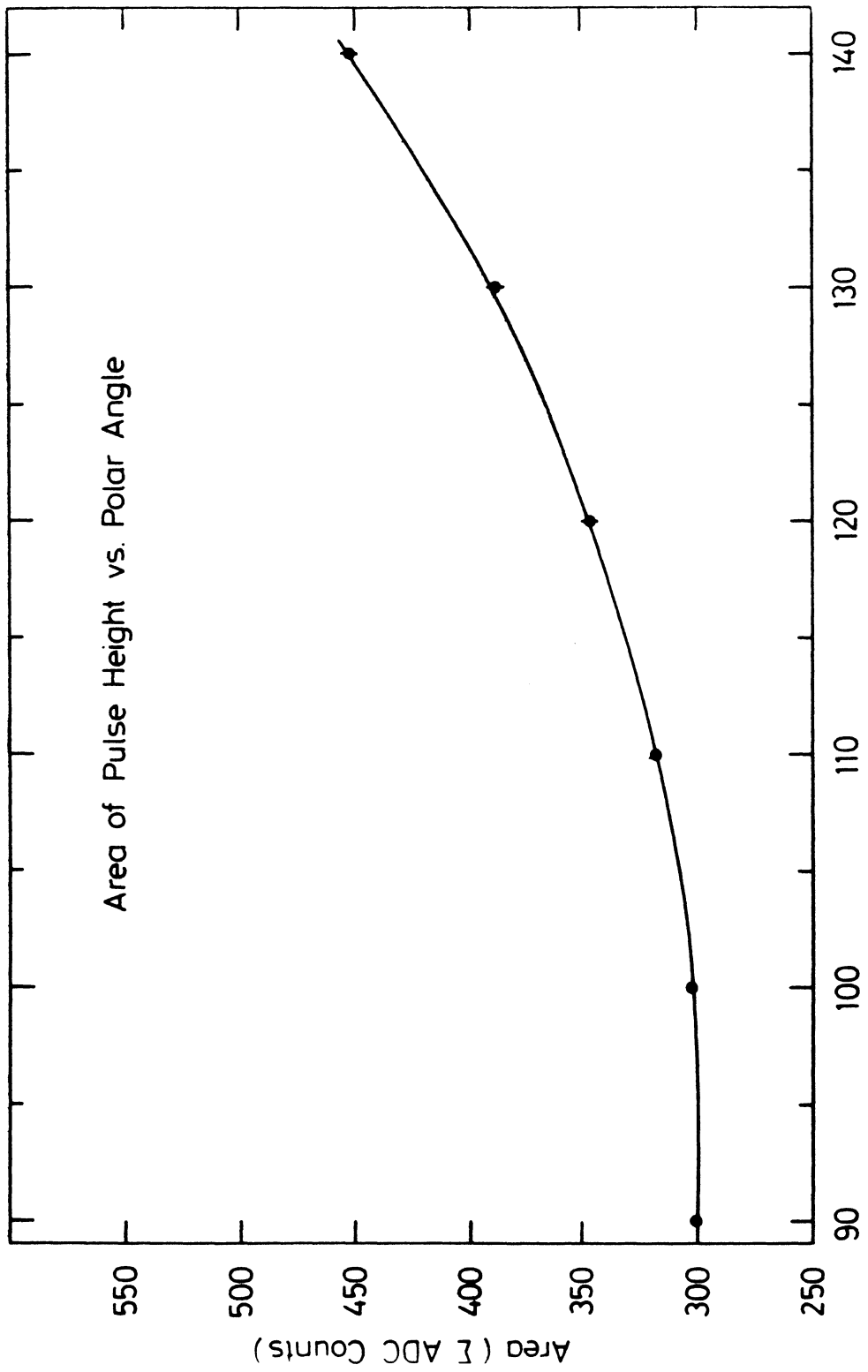
Area of Pulse Height vs. Polar Angle
Area (Σ ADC Counts)
550
500
450
400
350
300
250
90
100
110
120
130
140
Polar Angle Θ (degrees)

Figure 9d

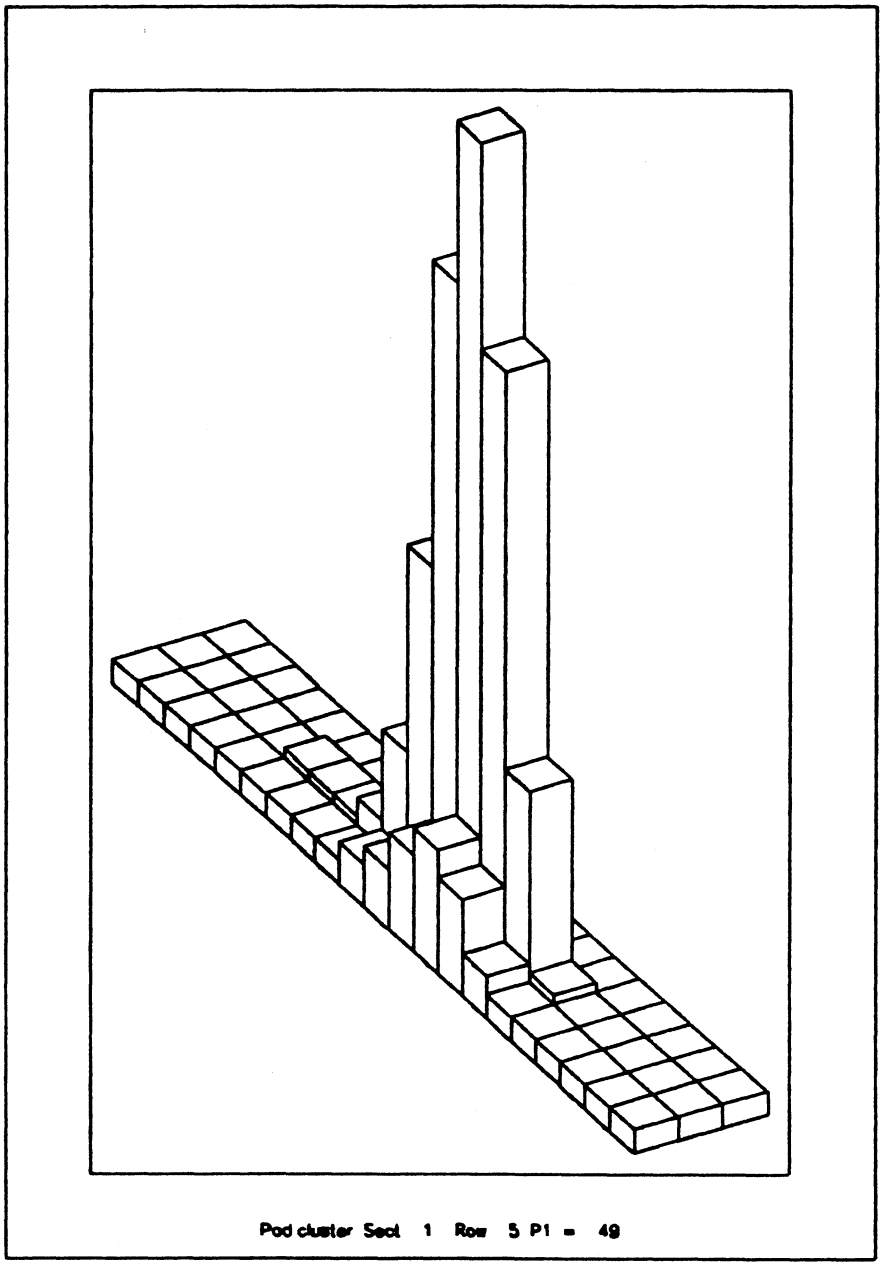
Pod cluster Sect 1 Row 5 P1 = 49
Pod number
51
50
49
2 8 11 8 4 2
1 21 65 88 70 36 13 3 1 1 1
2 8 11 8 4 2
231
241
Time slice

Figure 10a

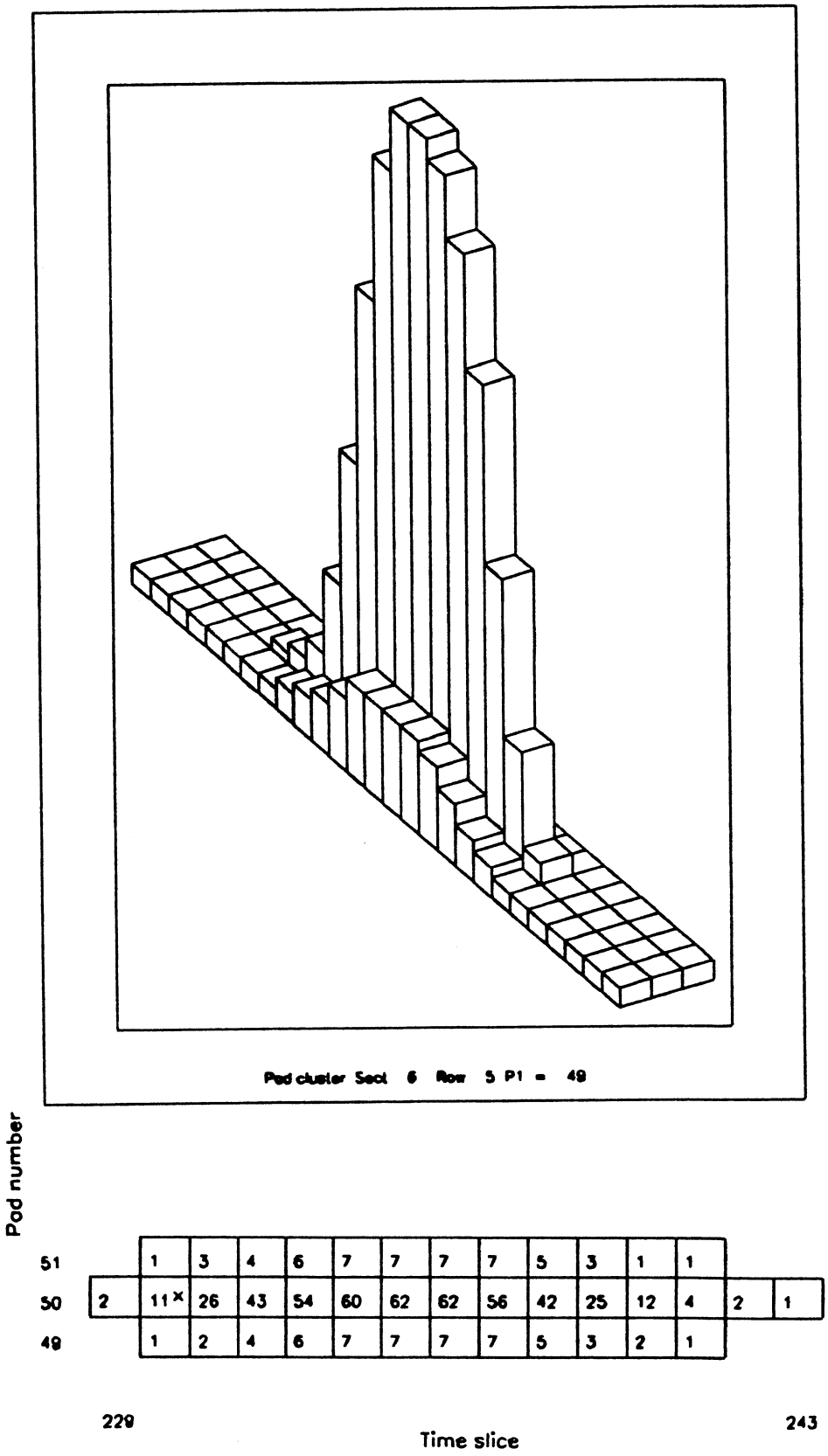
Pad cluster Sect 6 Row 5 P1 = 49
Pad number
51
50
49
1 3 4 6 7 7 7 7 5 3 1 1
2 11 26 43 54 60 62 62 56 42 25 12 4 2 1
1 2 4 6 7 7 7 7 5 3 2 1
229
243
Time slice

Figure 10b

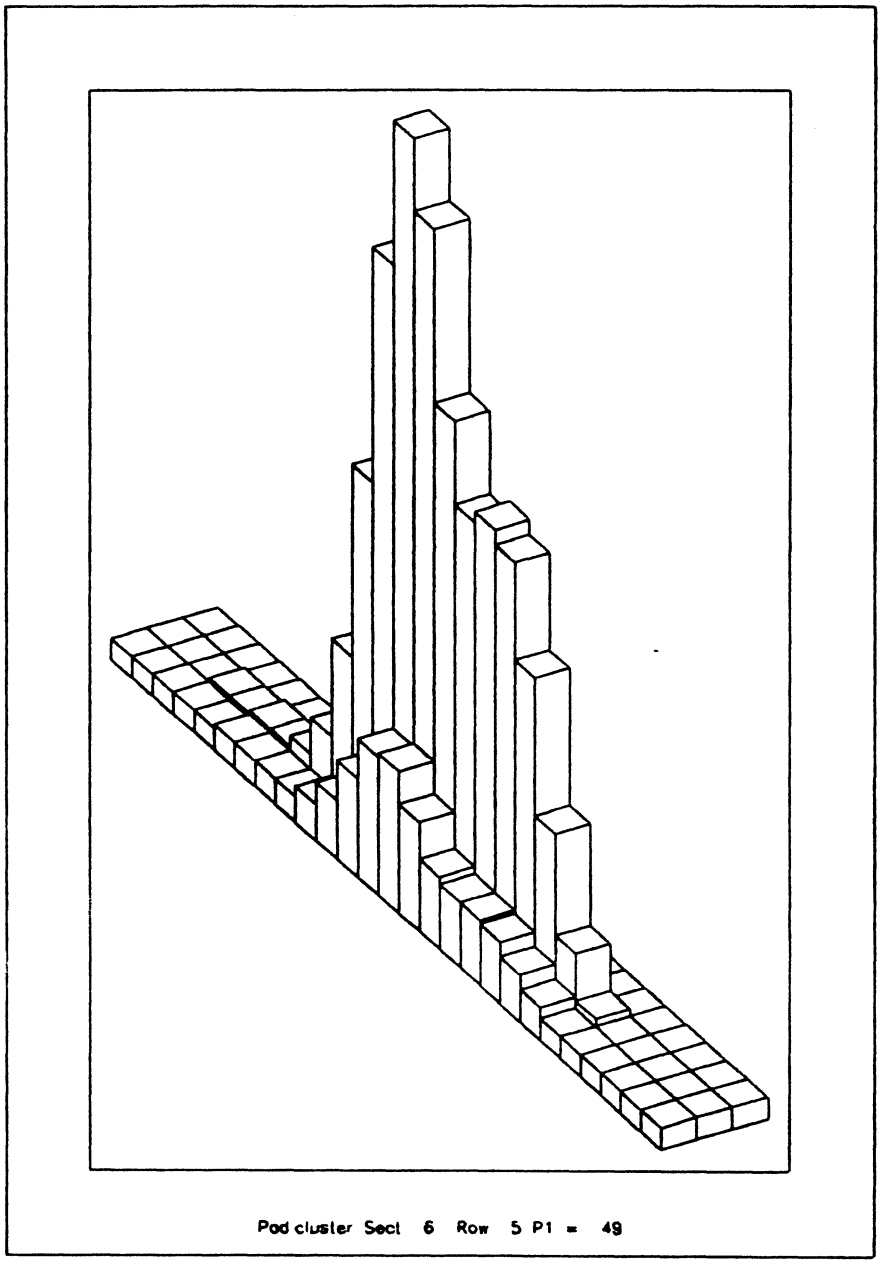

Figure 11

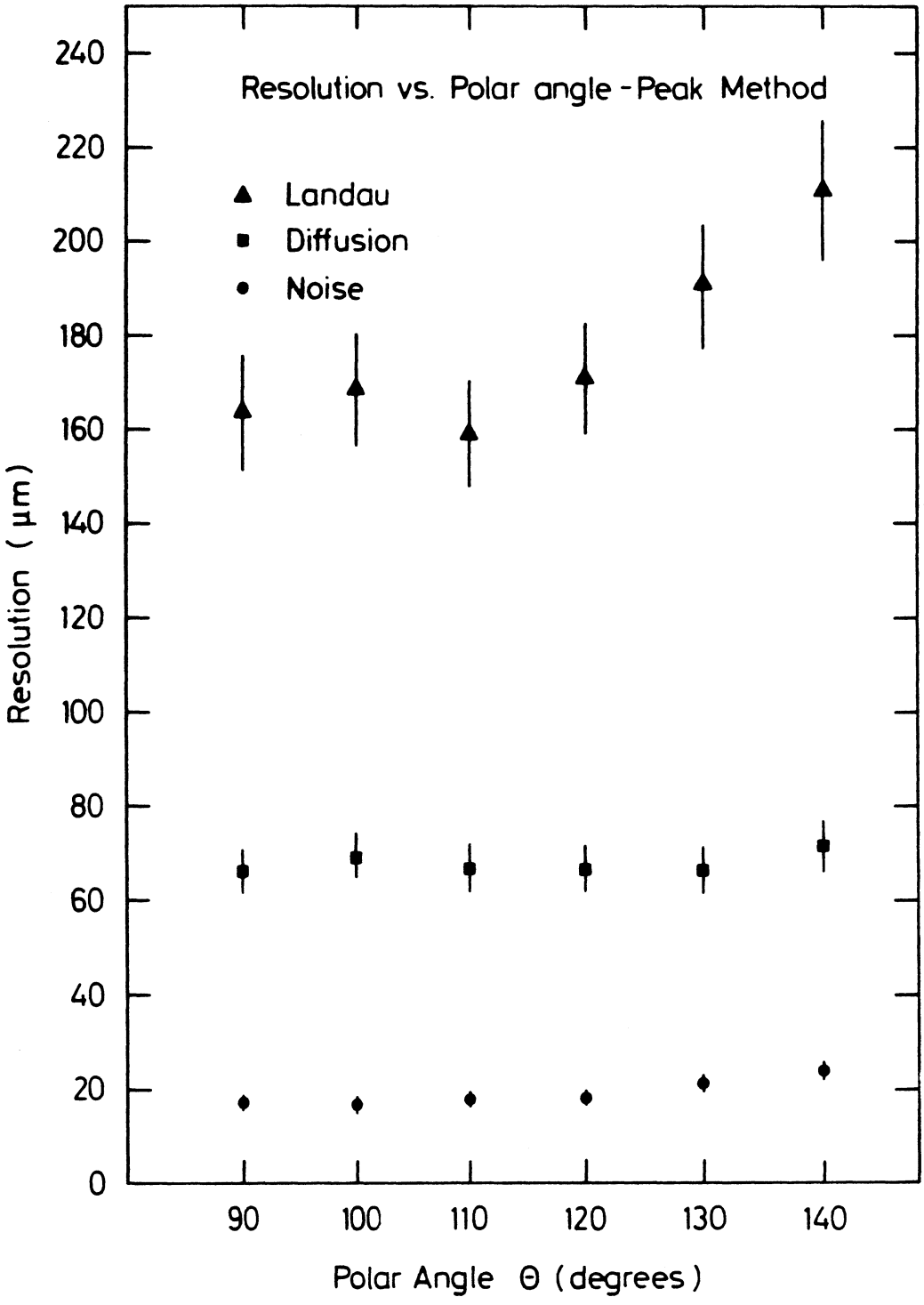
Resolution vs. Polar angle - Peak Method
Landau
Diffusion
Noise
Resolution (μm)
240
220
200
180
160
140
120
100
80
60
40
20
0
90
100
110
120
130
140
Polar Angle Θ (degrees)

Figure 12a

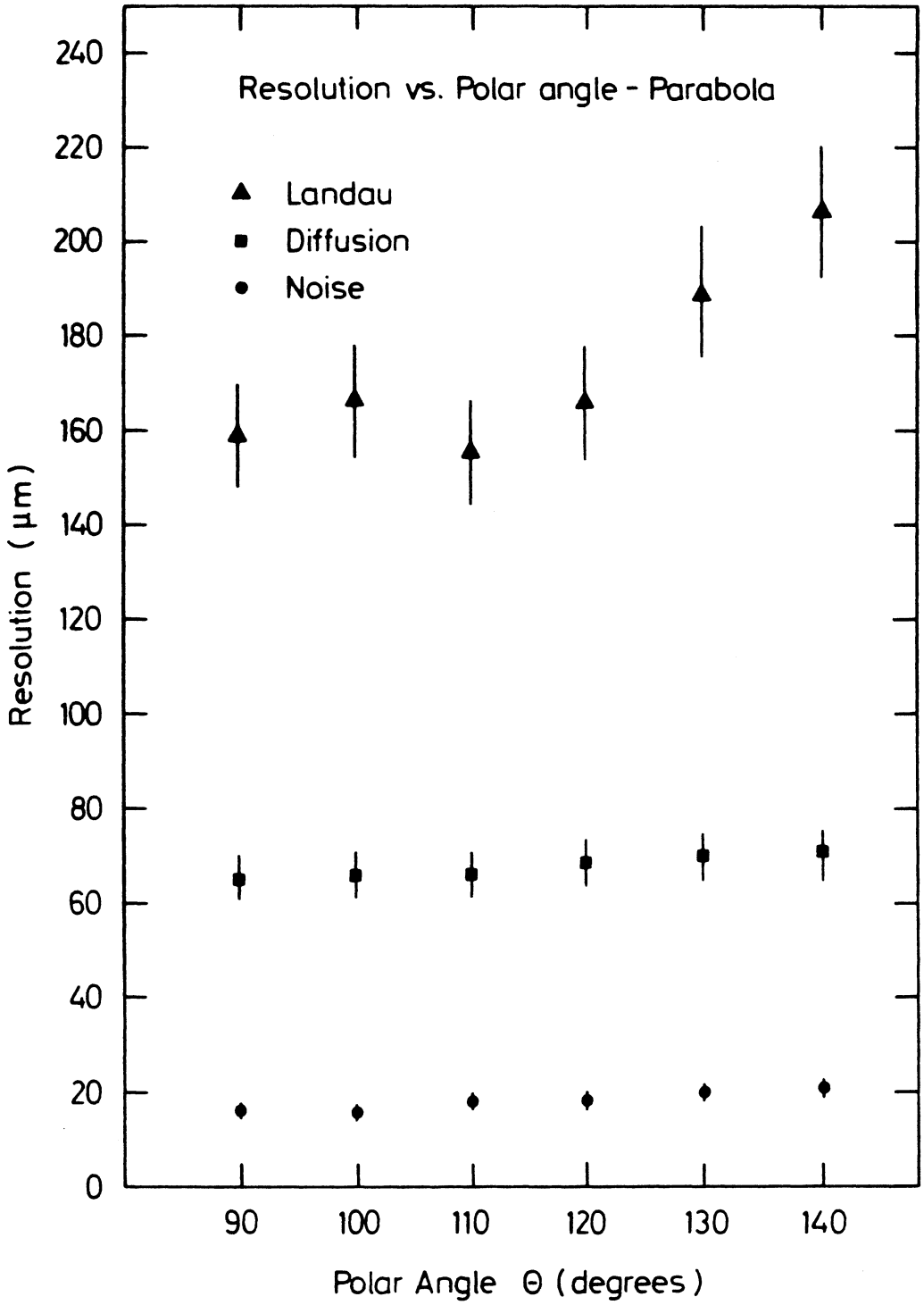
Resolution vs. Polar angle - Parabola
Landau
Diffusion
Noise
Resolution (μm)
240
220
200
180
160
140
120
100
80
60
40
20
0
90
100
110
120
130
140
Polar Angle Θ (degrees)

Figure 12b

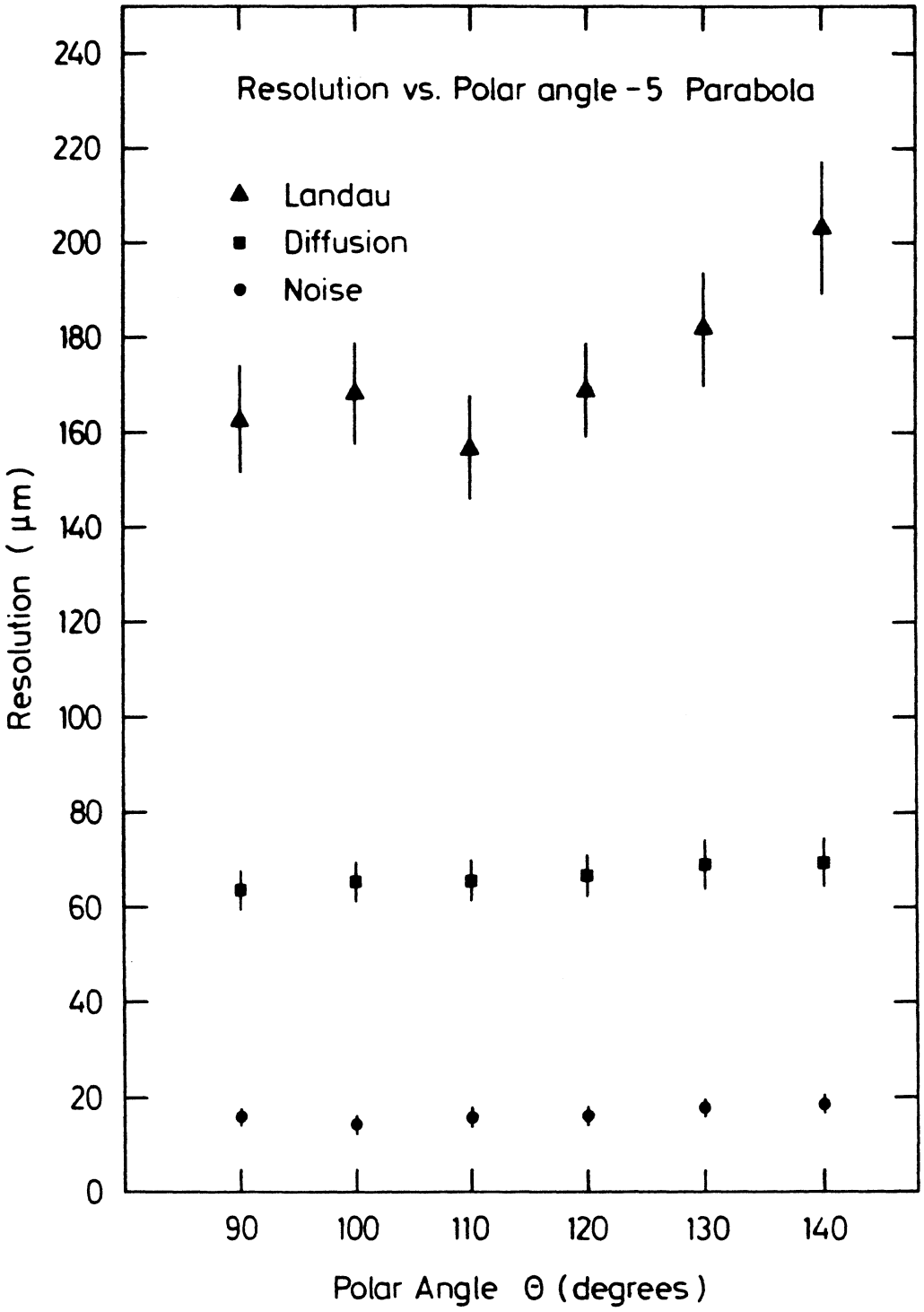
Resolution vs. Polar angle - 5 Parabola
Landau
Diffusion
Noise
Resolution (μm)
240
220
200
180
160
140
120
100
80
60
40
20
0
90
100
110
120
130
140
Polar Angle Θ (degrees)

Figure 12c

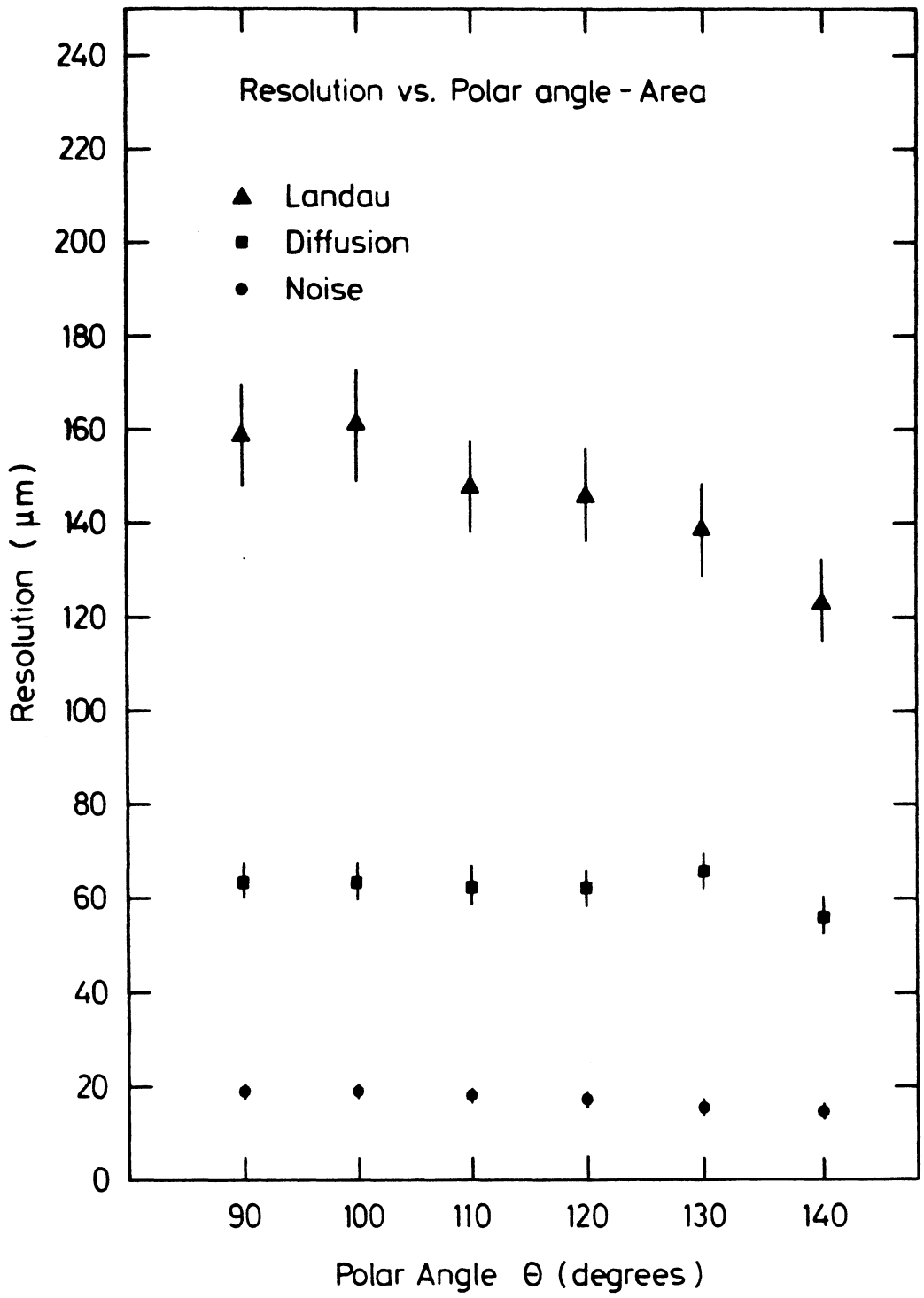
Resolution vs. Polar angle - Area
Landau
Diffusion
Noise
Resolution (μm)
240
220
200
180
160
140
120
100
80
60
40
20
0
90
100
110
120
130
140
Polar Angle θ (degrees)

Figure 12d

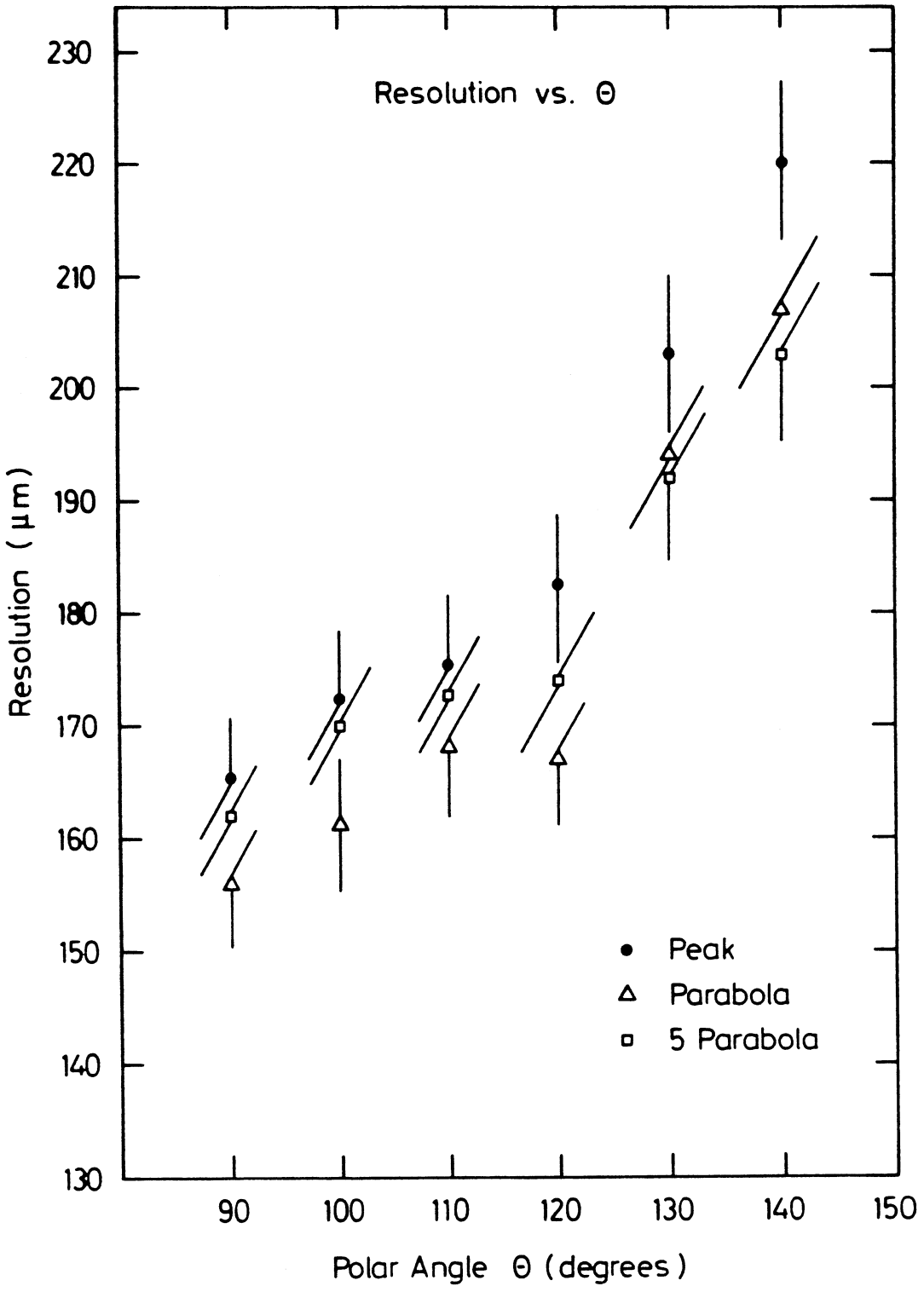
Resolution vs. Θ
Resolution (μm)
230
220
210
200
190
180
170
160
150
140
130
90
100
110
120
130
140
150
Polar Angle Θ (degrees)
Peak
Parabola
5 Parabola

Figure 13a

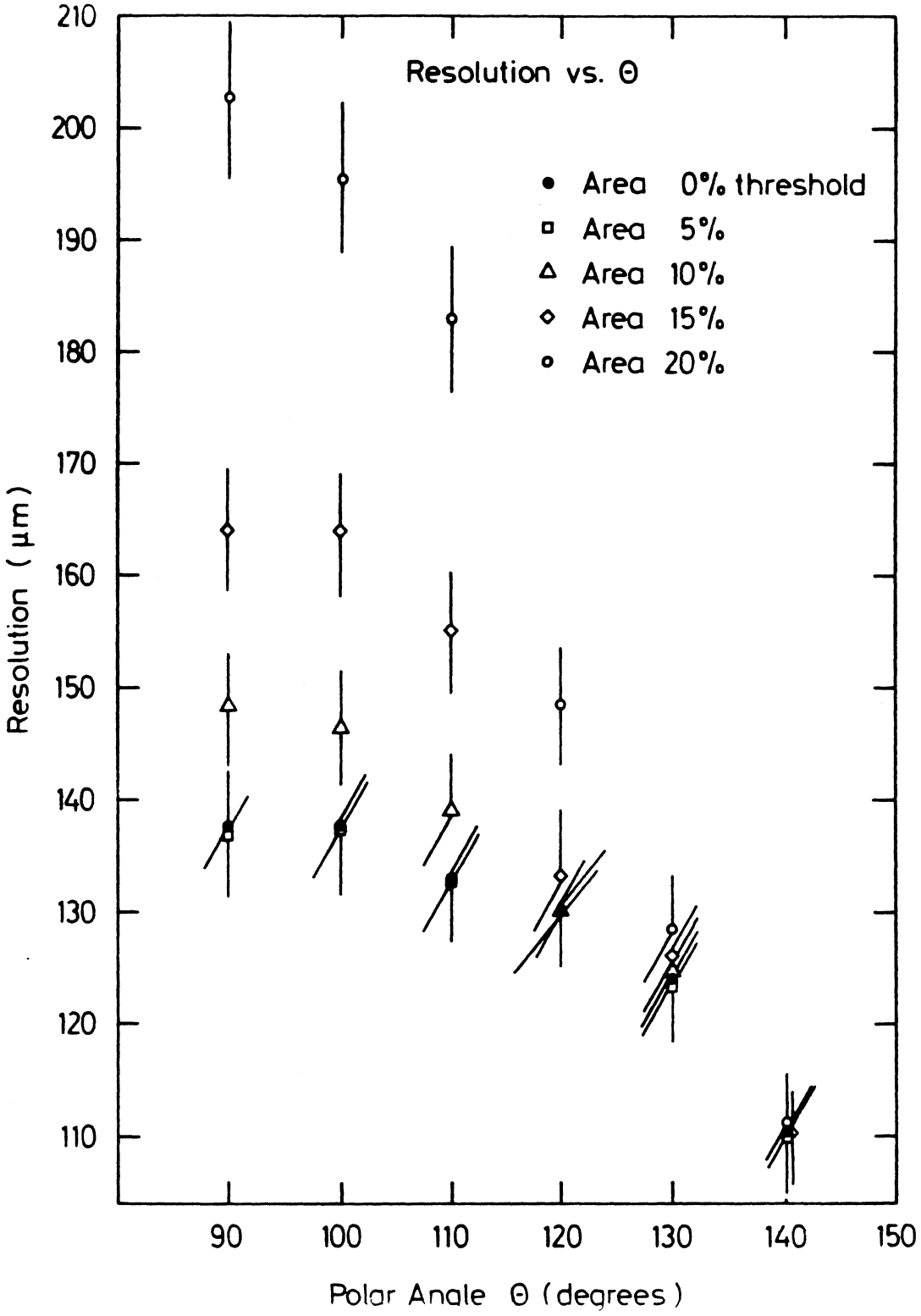
Resolution vs. Θ
Area 0% threshold
Area 5%
Area 10%
Area 15%
Area 20%
Resolution (μm)
Polar Angle Θ (degrees)
210
200
190
180
170
160
150
140
130
120
110
90
100
110
120
130
140
150

Figure 13b

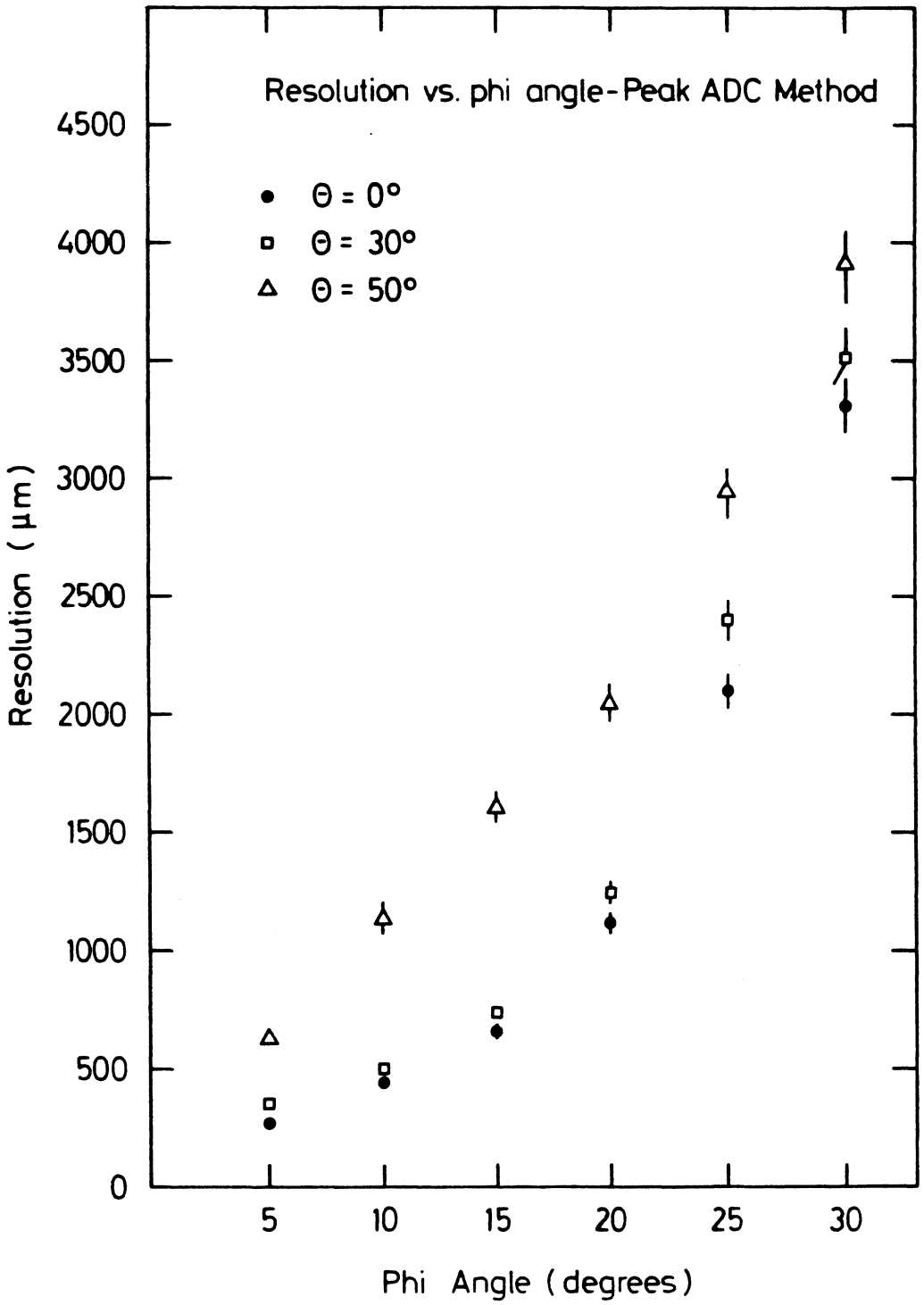
Resolution vs. phi angle-Peak ADC Method
Θ = 0°
Θ = 30°
Θ = 50°
Resolution (μm)
4500
4000
3500
3000
2500
2000
1500
1000
500
0
5
10
15
20
25
30
Phi Angle (degrees)

Figure 14a

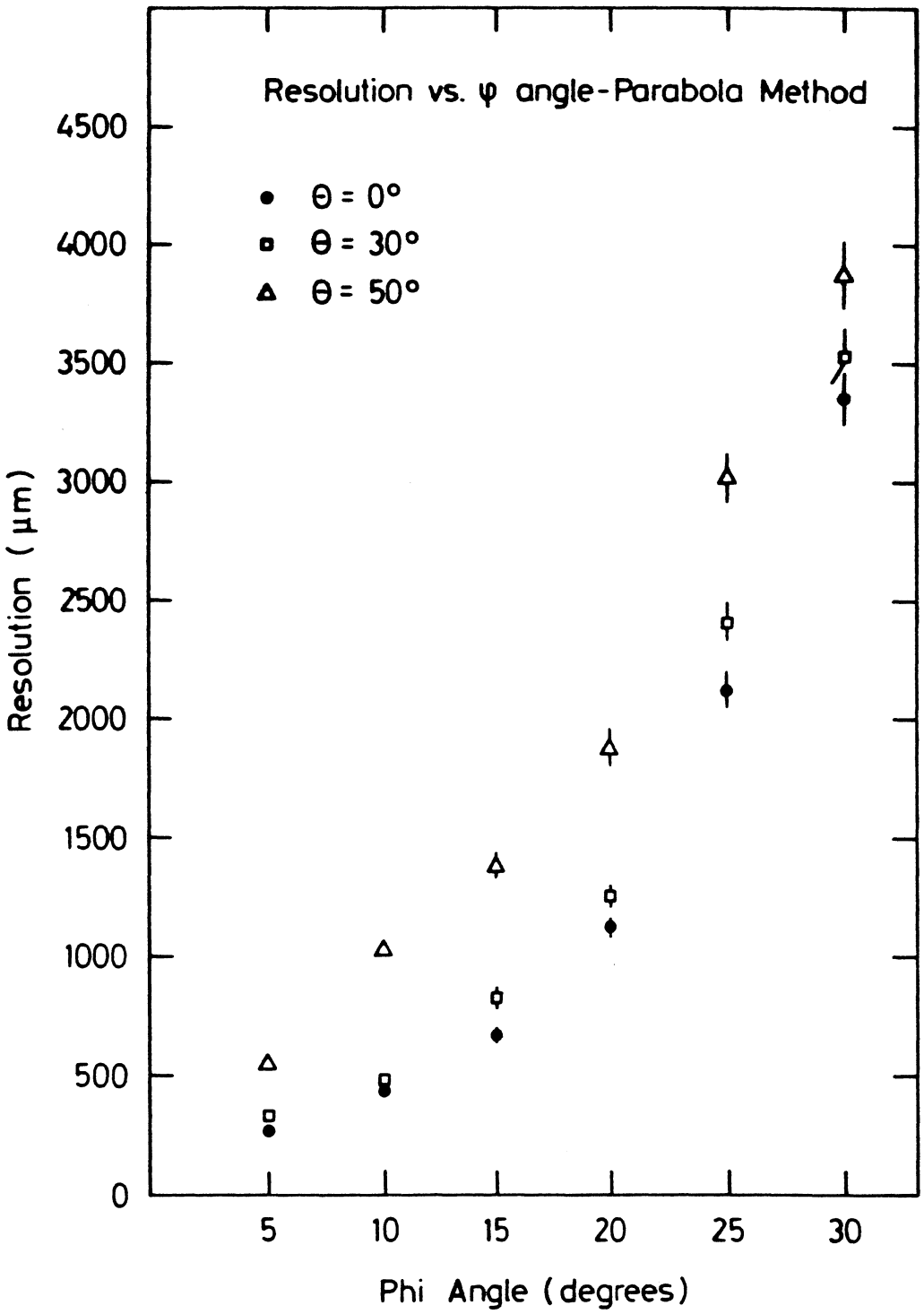
Resolution vs. φ angle-Parabola Method
Θ = 0°
Θ = 30°
Θ = 50°
Resolution (μm)
4500
4000
3500
3000
2500
2000
1500
1000
500
0
5
10
15
20
25
30
Phi Angle (degrees)

Figure 14b

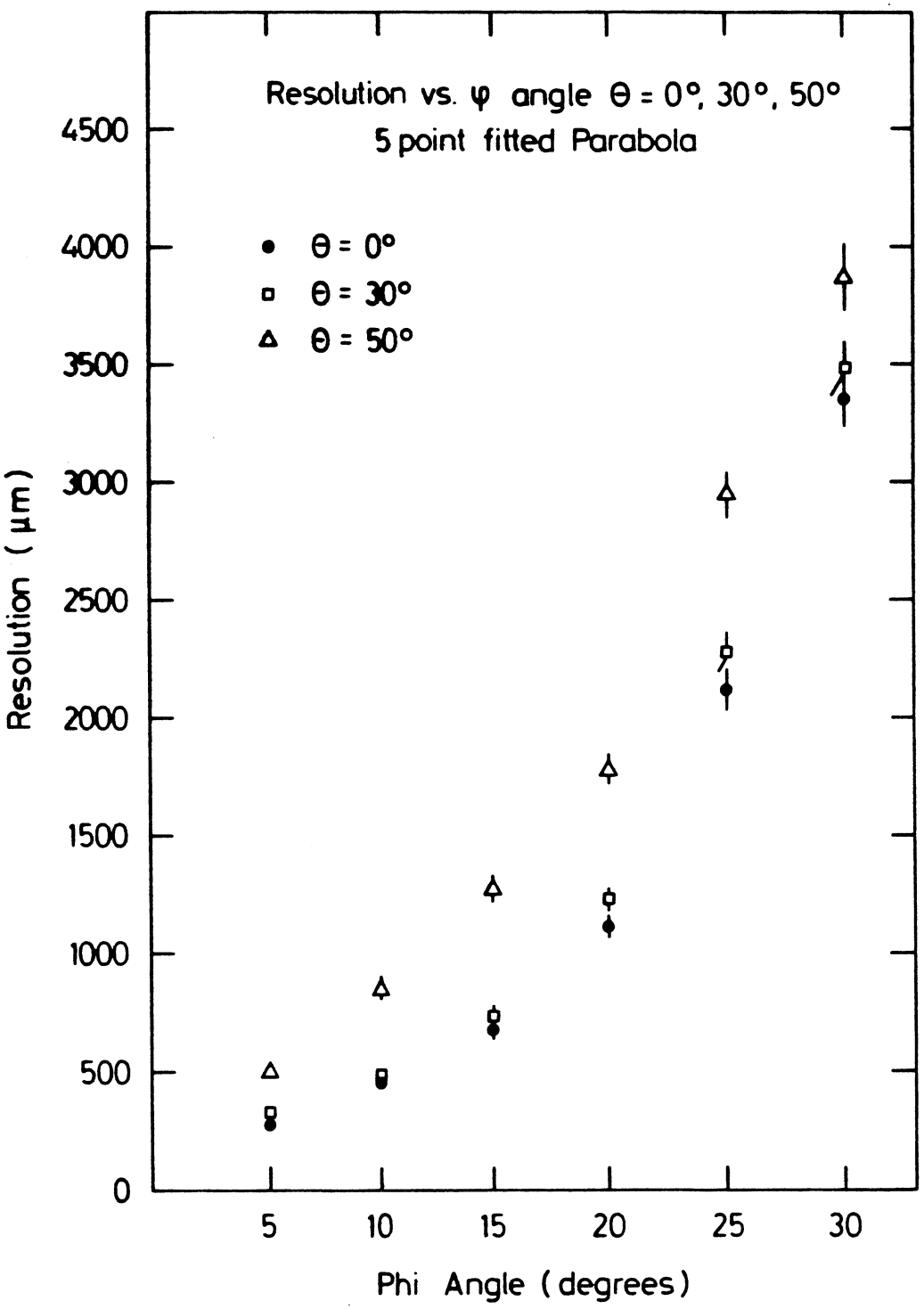
Resolution vs. φ angle Θ = 0°, 30°, 50°
5 point fitted Parabola
Θ = 0°
Θ = 30°
Θ = 50°
Resolution (μm)
4500
4000
3500
3000
2500
2000
1500
1000
500
0
5
10
15
20
25
30
Phi Angle (degrees)

Figure 14c

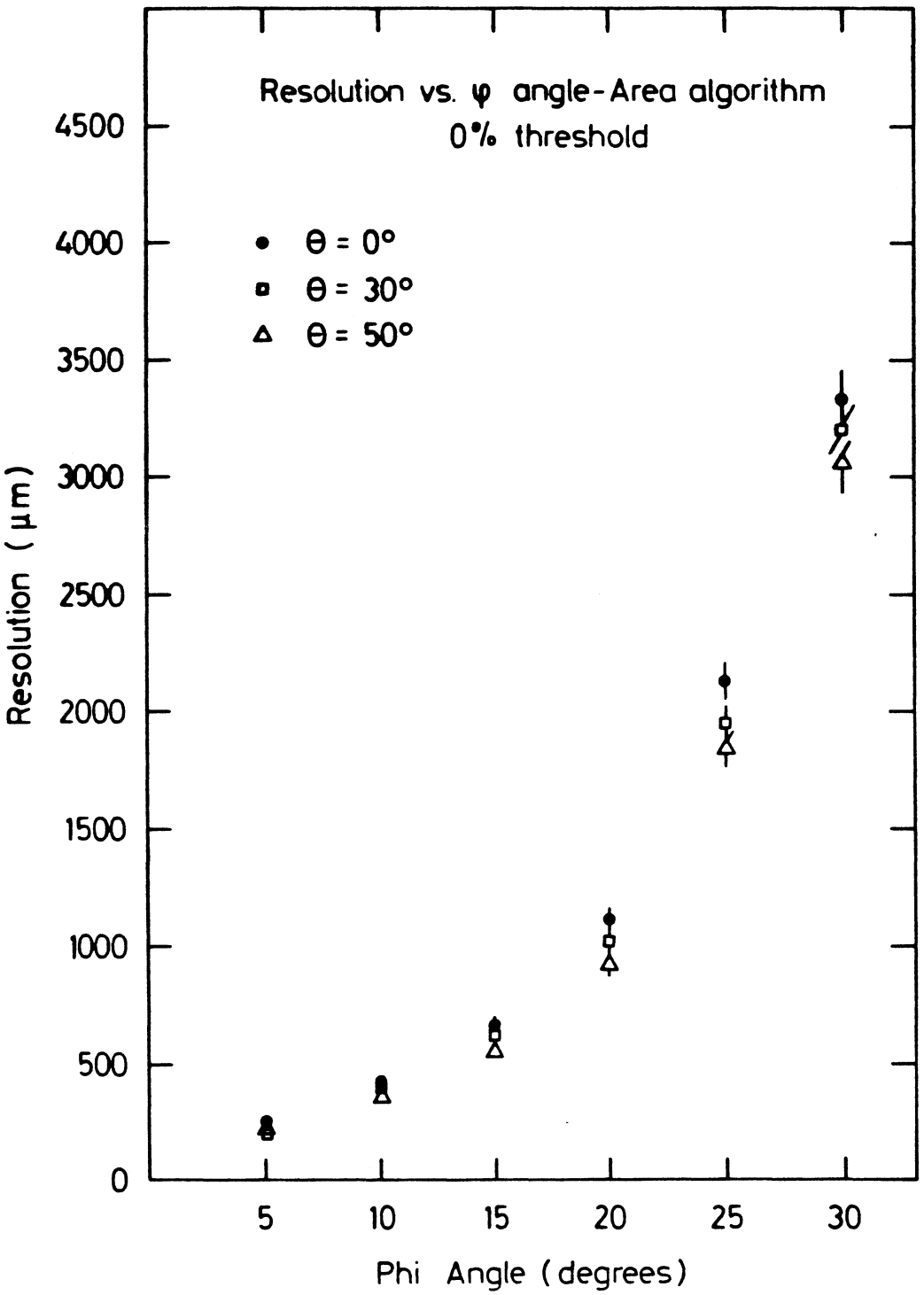
Resolution vs. φ angle-Area algorithm
0% threshold
θ = 0°
θ = 30°
θ = 50°
Resolution (μm)
4500
4000
3500
3000
2500
2000
1500
1000
500
0
5
10
15
20
25
30
Phi Angle (degrees)

Figure 14d

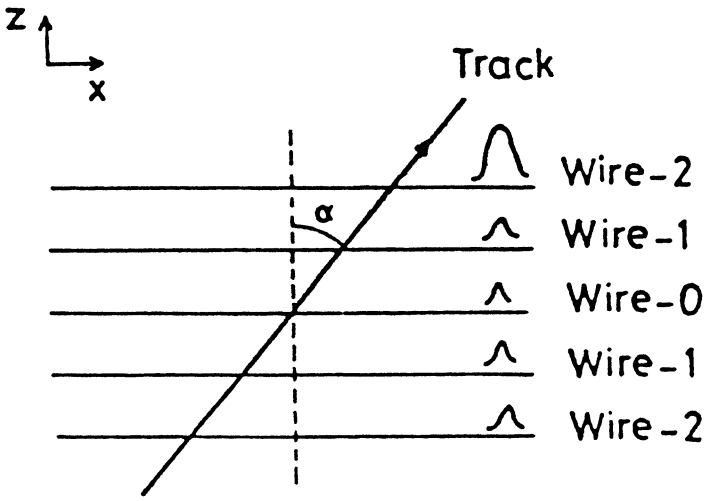

Figure 15

Table 1

cluster size (electrons)	probability for a minimum ionizing paricle
1	80.2
2	7.7
3	2.0
4	1.3
5	0.8
6	0.6
7	0.5
8	0.6
9	0.8
10	0.9
11	0.7
12	0.5
13	0.4
14	0.3
8-20	5.3
> 20	1.4
overflow	0.2

Table 2

Electron momentum	Mean Range	Min	Max
.05 (Mev/c)	.006 cm		
.1	.086	<.01	.14
.2	1.07	<.1	1.6
.5	16.6	<1.	27.
1.	82.8	10.	150.

Table 3 Variation of weights vs. Polar angle θ

Polar Angle (θ)	90	100	110	120	130	140
Top ADC	86.00 ± 1.87	84.75 ± 1.30	82.25 ± 1.47	77.25 ± 0.83	69.75 ± 0.43	62.00 ± 0.00
Parabola	87.39 ± 0.62	86.06 ± 0.31	83.34 ± 0.65	78.08 ± 0.20	69.96 ± 0.60	62.01 ± 0.02
5 Point Parabola	83.34 ± 0.89	82.22 ± 0.70	80.37 ± 0.60	76.24 ± 0.24	69.78 ± 0.49	62.33 ± 0.33
Area	300.25 ± 1.15	302.25 ± 0.73	318.25 ± 0.86	344.50 ± 0.41	388.50 ± 0.50	462.25 ± 0.11

Table 4 Resolution Results for Noise (μm)

Polar Angle (θ)	90	100	110	120	130	140
Top ADC	17.60 ± 1.25 ± 0.87	17.03 ± 1.21 ± 0.84	18.25 ± 1.28 ± 0.63	18.48 ± 1.30 ± 1.95	21.30 ± 1.50 ± 0.95	23.63 ± 1.66 ± 0.26
Parabola	16.83 ± 1.18 ± 0.80	16.30 ± 1.14 ± 0.91	17.75 ± 1.24 ± 0.45	17.80 ± 1.24 ± 1.51	20.40 ± 1.42 ± 1.07	21.40 ± 1.50 ± 0.93
5 Point Parabola	15.78 ± 1.10 ± 0.36	14.70 ± 1.04 ± 0.63	15.85 ± 1.12 ± 0.65	16.38 ± 1.14 ± 0.78	17.53 ± 1.22 ± 1.29	18.65 ± 1.30 ± 0.46
Area	19.93 ± 1.40 ± 0.46	19.05 ± 1.14 ± 0.39	18.70 ± 1.32 ± 0.52	17.55 ± 1.22 ± 0.71	15.80 ± 1.10 ± 0.72	14.93 ± 1.04 ± 0.56

Table 5 Resolution Results for Diffusion (μm)

Polar Angle (θ)	90	100	110	120	130	140
Top ADC	65.93 ± 4.62 ± 1.09	69.35 ± 4.86 ± 1.02	67.40 ± 4.72 ± 2.64	67.55 ± 4.72 ± 1.95	67.28 ± 4.72 ± 1.21	72.88 ± 5.10 ± 0.82
Parabola	65.70 ± 4.60 ± 1.10	66.50 ± 4.66 ± 1.62	66.68 ± 4.66 ± 2.43	68.73 ± 4.74 ± 2.12	70.00 ± 4.90 ± 1.01	71.30 ± 5.00 ± 1.51
5 Point Parabola	64.18 ± 4.50 ± 1.01	65.28 ± 4.58 ± 1.89	65.43 ± 4.58 ± 1.85	67.98 ± 4.76 ± 2.25	69.55 ± 4.86 ± 0.61	69.55 ± 4.86 ± 1.07
Area	63.43 ± 4.44 ± 1.46	63.18 ± 4.42 ± 0.58	62.25 ± 4.58 ± 1.19	62.45 ± 4.36 ± 0.35	66.00 ± 4.36 ± 0.53	56.50 ± 3.96 ± 1.28

Table 6 Resolution Results for Landau Fluctuations (μm)

Polar Angle (θ)	90	100	110	120	130	140
Top ADC	164.00 ±11.64 ± 1.73	168.00 ±11.93 ± 2.12	158.50 ±11.25 ± 1.50	170.75 ±12.12 ± 2.86	191.00 ±13.56 ± 2.55	211.75 ±15.03 ± 2.59
Parabola	159.00 ±11.29 ± 1.23	166.75 ±11.84 ± 1.30	155.25 ±11.02 ± 0.43	166.25 ±11.80 ± 1.09	188.00 ±13.35 ± 1.41	206.75 ±14.68 ± 1.64
5 Point Parabola	162.75 ±11.56 ± 0.83	168.00 ±11.93 ± 1.58	156.75 ±11.13 ± 1.09	168.25 ±11.95 ± 1.79	182.50 ±12.96 ± 1.50	203.25 ±14.43 ± 4.38
Area	159.50 ±11.83 ± 1.12	161.25 ±11.45 ± 0.83	147.25 ±10.46 ± 0.83	146.00 ±10.37 ± 1.23	139.00 ± 9.87 ± 0.00	123.50 ± 8.77 ± 1.12

Table 7 Resolution Results for Noise, Diffusion and Landau Fluctuations (μm)

Polar Angle (θ)	90	100	110	120	130	140
Top ADC	165.80 ± 5.80 ± 1.04	172.55 ± 6.04 ± 0.94	175.75 ± 6.15 ± 1.28	182.48 ± 6.39 ± 1.11	201.95 ± 7.07 ± 0.56	220.05 ± 7.70 ± 2.02
Parabola	156.43 ± 5.48 ± 2.06	161.63 ± 5.66 ± 1.60	168.13 ± 5.89 ± 0.36	167.58 ± 5.87 ± 1.43	194.38 ± 6.80 ± 0.88	207.05 ± 7.26 ± 1.99
5 Point Parabola	162.68 ± 5.69 ± 1.10	170.35 ± 5.96 ± 0.89	173.55 ± 6.07 ± 1.74	174.28 ± 6.24 ± 2.96	192.23 ± 6.73 ± 1.30	203.43 ± 7.12 ± 1.06
Area (0% Thres.)	137.88 ± 4.83 ± 0.29	137.73 ± 4.82 ± 0.52	133.78 ± 4.68 ± 0.35	130.00 ± 4.55 ± 0.51	124.63 ± 4.36 ± 0.56	111.58 ± 3.91 ± 0.93
Area (5% Thres.)	136.90 ± 4.79 ± 0.55	137.65 ± 4.82 ± 0.42	133.38 ± 4.67 ± 0.42	129.15 ± 4.52 ± 1.36	123.68 ± 4.33 ± 0.16	110.01 ± 3.85 ± 0.21
Area (10% Thres.)	148.35 ± 5.19 ± 1.18	146.75 ± 5.14 ± 0.95	139.15 ± 4.87 ± 2.56	129.93 ± 4.55 ± 0.42	124.15 ± 4.35 ± 1.36	109.83 ± 3.84 ± 0.38
Area (15% Thres.)	164.90 ± 5.77 ± 6.25	164.00 ± 5.74 ± 2.43	155.95 ± 5.46 ± 1.73	133.95 ± 4.69 ± 0.56	126.30 ± 4.42 ± 0.77	110.58 ± 3.87 ± 0.15
Area (20% Thres.)	203.90 ± 7.14 ± 3.44	195.96 ± 6.86 ± 1.45	183.28 ± 6.42 ± 2.23	148.50 ± 5.20 ± 0.50	128.75 ± 4.51 ± 0.63	111.53 ± 3.90 ± 0.30

References

[1] A. Caldwell, M. Mermikides, A. Peisert, R. Richter, L. Rolandi and M. Takashima, "TPC Simulation Program", ALEPH-TPC Note #85-10 (1985).

[2] F. Lapique and F. Piuz, "Simulation of the Measurement by Primary Cluster counting of the Energy lost by a Relativitic Ionizing Particle in Argon", Nucl. Instrum. and Methods 175 (1980) 297.

[3] J. Richstein, "Measurement of a Pad Response Function (PRF) by the use of a traversing Laser Beam in TPC90", ALEPH-TPC Note #84-25 (1984).

[4] A. Caldwell and M. Mermikides, "The TPC Resolution", ALEPH-TPC Note #85-20 (1985).

[5] H. Brettel, A. Peisert, R. Richter, "Long Pads in the TPC and the Electronics Response", ALEPH-TPC #83-4 (1983).

[6] R.C. Jared and M. Takashima, "An Algorithm to Generate Noise in the Time Domain", ALEPH-TPC #84-89 (1984).

[7] A. Hrisoho, "Time Domain Noise Calculation for the Common Base Current Amplifier Configuration", Nucl. Instrum. and Methods 185 (1981) 207.

[8] F.S. Goulding, "Pulse Shaping in Low-Noise Nuclear Amplifiers : A Physical Approach to Noise Analysis", Nucl. Instrum. and Methods 100 (1972) 493.

[9] M.O. Deighton, "A Time Domain Method for Calculating Noise of Active Integrators used in Pulse Amplitude Spectroscopy", Nucl. Instrum. and Methods 58 (1968) 201.